Department of Physics and Astronomy
University of Heidelberg

Bachelor thesis in Physics
submitted by

Nikolai Bolik

born in Aachen

2022

Topological phases and symmetries in 1D quantum walks

This Bachelor thesis has been carried out by
Nikolai Bolik
at the
Institute for Theoretical Physics in Heidelberg
under the supervision of
Sandro Wimberger

Abstract

Recently [Phys. Rev. Lett., 121:070402, Aug 2018] a quantum kicked rotor walk has been implemented in momentum space by loading a ^{87}Rb Bose-Einstein condensate into an optical pulsed lattice. The experimental results showed overall good agreement with the theoretical predictions but also differed in the details. A complementary argument to previous explanations will be given, consulting light shift induced effects and dispersive properties of the system for causing the observed discrepancies.

Furthermore, from the field of mathematics topological principles have been passed on to physics. For example the quantum hall effect can be understood in terms of Chern numbers as topological invariant. It has been recognized that periodically driven quantum systems have the capacity to resolve the unconventional topological matter. The double kicked quantum rotor with internal spin 1/2 degree of freedom is such a system, displaying a connection between topologically protected edge states and the topologically invariant winding number.

The mean chiral displacement is an experimentally obtainable observable that converges onto the winding number. This offers interesting possibilities for measuring topological phase transition. Recognizing these possibilities, investigations regarding the feasibility will be presented, suggesting a new protocol for an experimental implementation.

In [Phys. Rev. Lett., 121:070402, Aug 2018] wurde über einen im Impulsraum implementierten gekickter Quanten-Rotator Zufallsprozess mit einem ^{87}Rb-Kondensat in einem optisch gepulsten Gitter berichtet. Insgesamt stimmte das experimentelle Ergebnis gut mit den zugrundeliegenden theoretischen Vorhersagen überein, jedoch wurden auch Unterschiede in den Details beobachtet. Zu den bereits bestehenden Ausführungen wird eine komplementäre Erklärung abgegeben, welche den Grund der bestehenden Diskrepanzen in „light shift" induzierten Effekten, sowie den dispersiven Eigenschaften des Systems sucht.

Aus dem Gebiet der Mathematik heraus haben sich topologische Grundsätze auch zur Physik durchsetzen können. So kann zum Beispiel der Quanten-Hall-Effekt mithilfe von Chernklassen als topologische Invarianten beschrieben werden. Es blieb nicht unbemerkt, wie Systeme unter periodischer Entwicklung die Möglichkeit besitzen, unkonventionelle Arten der Materie mit topologischen Eigenschaften herbeizuführen. Der doppelt gekickte Quanten-Rotator mit einem internen Spin 1/2 Freiheitsgrad ist ein solches zeitlich periodisch entwickeltes System, welches einen Zusammenhang zwischen topologisch geschützten Randzuständen und der topologisch invarianten Windungszahl besitzt.

Das experimentell zugängliche „mean chiral displacement" ist eine Observable, die hin zur topologisch interessanten Windungszahl konvergiert. Dies öffnet Türen für experimentelle Vermessungen topologischer Phasenübergänge. Aufbauend auf diesen Möglichkeiten werden Optionen zur Realisierbarkeit eines solchen Experimentes ausgelotet und in deren Konsequenz ein neues experimentelles Protokoll vorgeschlagen.

Contents

Introduction

Motivation

The striking differences of quantum walks to their classical counterpart have proven themselves to be fruitful ground for computer science applications. Due to interference along the path quantum walks demonstrate drastically different outcomes compared to classical random walks. One of those main differences is that compared to the classical counterpart, a particle in a quantum walk is by measurement on average expected to end up further away from the origin. This offers possibilities for algorithms with up to exponentially faster runtime. [1]

For actual experimental applications in the field of quantum computation, decoherence poses an issue independently of the concrete implementation. In order to overcome the unavoidable problems of perturbations and decoherence in future experiments, topological phases might play a vital role. The recognition of topological phases [2] finds application in so called „topological insulators", revealing topologically protected edge states. The stability of the topological invariant is translated upon these edge states, causing them to be stable towards a great variety of perturbations.

Within this work, we will concentrate on the realization of quantum walks and topological phase transitions in quantum kicked rotor configurations. The quantum kicked rotor is a toy system, that displays a large range of dynamic properties and is experimentally accessible. The ambition is to accomplish a better understanding of these systems and to lay some theoretical groundwork for possible future experimental implementations, especially in the domain of topological phases.

Outline

This thesis deals mainly with two subjects. On the one hand, we will give reinterpretation for an already existing quantum walk experiment in momentum space. [3, 4] On the other hand, we will present a proposal for a possible experimental realization measuring topological phase transitions in a spin $1/2$ Floquet system, building upon the groundwork already set in Ref. [5, 6].

In the first chapter the theoretical background on quantum kicked rotor walks as an approximation to ideal quantum walks will be discussed. Building upon this, the second chapter deals with the relevant background on topological phases in quantum systems.

As already hinted above, the third chapter will present an elementary reinterpretation of a quantum walk experiment, attempting to resolve discrepancies between theoretical predictions and experimental results, discussed in Ref. [3]. Most importantly, the ambition is to explain the discrepancies without additional physical assumptions beyond effects intrinsic to the experiment. We will understand the observed experimental effects as a result of dispersion in the system, highlighted by light shift induced alterations of the experimental protocol and a narrow initial ratchet state in momentum space.

In the fourth chapter, we will discuss possibilities for how an experimental protocol measuring topological phase transitions from Ref. [5] could be implemented. Also, the system will be tested for stability in phase fluctuations that arise due to the experimental setup. The results will advocate the possibility that such a system might meet successful experimental realization, if discussed experimental effects would be sufficiently controlled.

Finally a brief summary will be given.

1 Theoretical background on discrete time quantum walks

Model variables might be described in continuous time or in discrete time. For a continuous-time model, time is considered to flow on the real number line. Consequently, a continuous-time process allows principally for events to occur at arbitrary times. For a discrete-time process, in contrast, events would be considered to happen at separate and distinct points in time. Such a process would be a sequence of events happening at singular points in time. One might imagine an analog clock with continuously moving pointers, compared with a digital clock with its display indicating the passing of time by jumping from one number to the next. Random walk processes can be described too as being continuous or discrete in time. Furthermore, we restrict ourselves to discrete-time random processes, meaning that the process consists of a succession of random processes which happen at discrete points in time.

1.1 Quantum walks

Quantum walks are the quantum mechanical analog to the classical random walks. In a random walk, the „walker" traverses a given graph on a random trajectory. At each knot within the graph, he decides based on assigned probabilities which will be the next knot in his journey. In the simplest case, this corresponds to a one-dimensional walk on integer numbers $\mathbb{Z}$, in which the walker decides to go either left or right, while his decision is made by a coin toss ($p = 1/2$). By the central limit theorem, the probability distribution converges both in time average or in ensemble average to a gaussian distribution that expands diffusively in the walk-space as time continues.

In the quantum mechanical formulation, the process has to be understood as a sequence of operators. A detailed introduction on quantum walks can be found in Ref. [1]. In such a walk the quantum system can traverse all possible paths at the same time with a certain probability. Due to this, the different paths can interfere with themselves, and new kinds of physics can form. In the operator sequence evolving the system, one step consists of a coin and a step operator. The quantum system must provide an internal degree of freedom (DOF) upon which the coin operator acts and an external DOF on which the step operator can perform. An example would be a system with an internal spin-1/2 DOF that evolves on an external lattice structure e.g. in momentum space, as has been experimentally implemented in Ref. [4]. For the interested reader, further experimental implementations might be found in Ref. [7–24].

The coin operator mixes the internal quantum states at each position while the step operator shifts the internal states respectively to an accessible position in the external DOF. We call a coin balanced if the probability stays evenly distributed on the internal degrees of freedom (DOF) after the mixing by the operator. Well known balanced coins for a two state system with internal states $|1\rangle \equiv \binom{0}{1}$ and $|2\rangle \equiv \binom{1}{0}$ are the Hadamard coin $\hat{H}$ or the beamsplitter matrix $\hat{Y}$.

$$\hat{H} = \frac{1}{\sqrt{2}} \begin{pmatrix} 1 & 1 \\ 1 & -1 \end{pmatrix} \qquad \hat{Y} = \frac{1}{\sqrt{2}} \begin{pmatrix} 1 & i \\ i & 1 \end{pmatrix} \tag{1}$$

Denoting the external states by $|n\rangle$, the step operator in 1D that links external states separated by d knots on the lattice is given by:

$$\hat{S} = |2\rangle\langle 2| \otimes \sum_n |n+d\rangle\langle n| + |1\rangle\langle 1| \otimes \sum_j |n-d\rangle\langle n| \tag{2}$$

$$= \exp\left(-i\hat{n}d \cdot \sigma_z\right) \tag{3}$$

Here σ_z features the third Pauli-matrix. The most usual case is reflected by a step operator that couples neighbored knots $d = 1$ in the external DOF. Frequently for initializing such a discrete-time quantum walk, a different coin than the one used for the walk is used as gate. From this perspective, by the equations given above, two protocols would be conducted. For a quantum walk consisting of j steps one might implement $\hat{U}_{step} = [\hat{Y}\hat{S}]^j\hat{H}$, or $\hat{U}_{step} = [\hat{H}\hat{S}]^j\hat{Y}$. The final probability distribution is then given by $P(n,j) = P_{|1\rangle}(n,j) + P_{|2\rangle}(n,j)$. Both walk protocols are shown in Fig. 1.

Such a walk features ballistic expansion in the external DOF, corresponding to quadratic speedup compared to the diffusive expansion of the classical counterpart. Note that due to the deterministic nature of quantum mechanics the randomness enters the system only in the measuring process. If a random walk approach for quantum computer algorithms is taken, this quadratic speedup in the expansion of the walk could even lead up to exponential speedup in the algorithm, as described in Ref. [1, 25]. This bridge between the abstract and the practical makes quantum walks a thrilling and promising field of research.
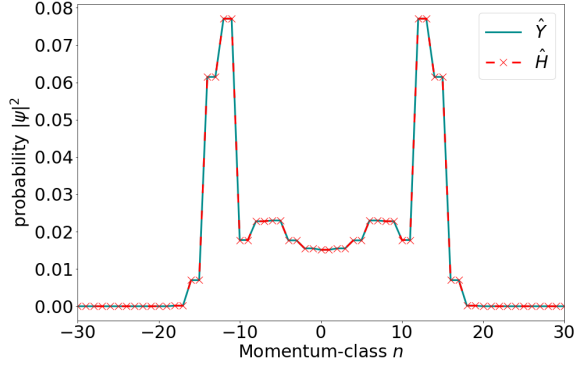
Figure 1: The figure shows the ideal quantum walk, implemented with the initial state $|\psi\rangle_{in} = |2\rangle \otimes (|1\rangle + |2\rangle)$. The figure compares both protocols explained above. $\hat{H}$ denotes the protocol initialized by the $\hat{Y}$-coin and executed with the $\hat{H}$-coin, $\hat{Y}$ vice versa. It is demonstrated that the ideal quantum walk does not distinguish between the balanced coins. Here the external state is a lattice in momentum space. The walk is depicted for $j = 20$ steps in the evolution.

1.2 Quantum kicked rotor

1.2.1 Quantum kicked rotor introduction

The quantum kicked rotor (QKR) is the quantum mechanical analog to the classical kicked rotor model. The classical kicked rotor model describes a particle that is restricted to a ring. A homogeneous field is periodically switched on for an infinitesimally short time, kicking the particle. Therefore the strength of the kick depends on the particle's position on the ring. The Hamiltonian to describe the system reads as:

$$\mathcal{H} = \frac{1}{2}p^2 + k\cos(\theta) \sum_{n=-\infty}^{\infty} \delta(t - n\tau) \tag{4}$$

p being the momentum of the particle, k represents the strength of the kick, θ is the angle concerning the orientation of the kicking field, and τ denotes the time between the kicks.

The problem however can be mapped to a line by interchanging the characteristics of ring and potential. In this scenario, the kick potential itself has periodic properties and thus the kick strength itself is dependent on the position θ. Since the particle is restricted to a line, it experiences the same kick-strength whenever it has passed an entire period of the kick potential of $\theta = 2\pi$. Therefore it is $\theta = x \mod(2\pi)$.

The Hamiltonian for the quantum mechanical analog to the problem can be found by the correspondence principle.

$$\hat{\mathcal{H}} = \frac{1}{2}\hat{p}^2 + k\cos(\hat{\theta}) \sum_{n=-\infty}^{\infty} \delta(t - n\tau) \tag{5}$$

Here the momentum operator $\hat{p}$ and the angular momentum operator $\hat{\theta}$ satisfy the canonical permutation relation. With the Hamiltonian one can compute the one cycle Floquet operator for the time evolution of the system. As the system has a time-dependent Hamiltonian one has to consider the Dyson series.

$$\begin{aligned}
\hat{U}(t + \tau, t) &= \hat{T}\exp\left(-i \int_t^{t+\tau} \hat{\mathcal{H}}(t')dt'\right) \\
&= \exp\left(-i\frac{\hat{p}^2}{2}\tau\right) \cdot \exp\left(-ik\cos(\hat{\theta})\right)
\end{aligned} \tag{6}$$

Here $\hat{T}$ denotes the time ordering operator. The one-period evolution operator fractures into a part that resembles the kick and into a part that resembles the free evolution of the system in between the kicks. Depending on the choice of the parameters k and τ the model is able to display dynamical localization

with stagnation in energy growth, anti-resonant behavior with the system not evolving at all, and resonant behavior with quadratic growth in energy. A quadratic increase in energy corresponds to a ballistic expansion in momentum space. As discussed in Sec. 1.1, a ballistic expansion is a signature of the quantum walks.

1.2.2   Rewriting free evolution operator

Due to the 2π periodicity of the potential, the Bloch theorem states that a basis of wave functions exists, which are a solution to the Schrödinger equation. These solutions are given by:

$$\psi(x,t) = e^{-i\beta x}\psi_\beta(x,t) \tag{7}$$

Within this equation, the second component ψ_β is, just as the potential periodic in x with the same period. Even more importantly, the theorem implies that within our dimensionless units momentum fractures into an integer part n and a non-integer part $\beta \in [0,1)$ that is conserved. This conserved part will furthermore be called quasimomentum.

$$p = n + \beta \tag{8}$$

This provides a lattice structure within momentum space, which becomes especially clear if one considers $\beta = 0$. The free evolution operator may be rewritten, in the following way:

$$\exp\left(-i\frac{\hat{p}^2}{2}\tau\right) = \exp\left(-i\frac{(\hat{n}+\beta)^2}{2}\tau\right). \tag{9}$$

Note that for zero quasimomentum $\beta = 0$ the free evolution operator becomes unity if $\tau = 4\pi$. A free evolution of $\tau = 4\pi$ corresponds to a full Talbot period. Since the free evolution operator does not contribute an additional phase and the evolution of the system is strictly given by the kick operator, this configuration is called resonant.

The introduction of quasimomentum accounts for the finite temperature of the system but is also slightly violating the resonance condition. As will be seen later on several occasions, the overall behavior of the system is not changed, if these perturbations are sufficiently small. In case of strong violation of the resonance condition, e.g. by arbitrarily choosing $\tau = 7/5$, the system experiences localization and stops to evolve rather quickly. This being said to point out that respecting the resonance condition is of great importance for an actual dynamically evolving system.

For a more detailed introduction to the quantum kicked rotor, Ref. [26–28] have been of use. For reverting the theoretically chosen unit system back to experimental units consult Ref. [28, 29].

1.2.3   Quantum kicked rotor walks

The underlying system to the discrete-time quantum kicked rotor walk is the QKR. The system described in Sec. 1.2 is expanded to a two-state system, since a true quantum walk demands an internal DOF, as described in Sec. 1.1.

$$\hat{\mathcal{H}} = \frac{1}{2}\hat{p}^2 \otimes \mathbf{1} + k\cos(\hat{\theta}) \sum_{n=-\infty}^{\infty} \delta(t - n\tau) \otimes \sigma_z \tag{10}$$

From the perspective of the discrete-time quantum walk, the Floquet-operator acting on the external DOF is to be understood as the step operator. As described in Sec. 1.2.2, the choice of $\tau = 4\pi$ and assuming $\beta = 0$ yields the resonant step operator.

$$\hat{\mathcal{U}}_{step} = \hat{\mathcal{U}}_f\hat{\mathcal{U}}_k = e^{-i\tau\frac{\hat{p}^2}{2}\otimes\mathbf{1}}e^{-ik\cos(\hat{\theta})\otimes\sigma_z}$$

$$\stackrel{\tau=4\pi}{=} \begin{pmatrix} e^{-ik\cos(\hat{\theta})} & 0 \\ 0 & e^{ik\cos(\hat{\theta})} \end{pmatrix} \tag{11}$$

Rewriting the kick operator like this, it becomes clear that the internal states experience a kick in opposite directions. Compared with the step operator from the ideal quantum walk in Eq. (2), this operator does not uniquely couple neighboured momentum classes. Dependent on the kick strength k this operator couples several momentum classes at once. In Ref. [30] a range for values of $k \in [0.75 : 2.75]$ is found in which the

operator creates a good overlap between neighboured momentum classes. For smaller k, the walk becomes too „lazy“, meaning that it barely evolves since the strongest coupling of a state is with itself. For too strong k, the momentum classes which are too far away from the neighboured one and all those in between are involved in the coupling. Thus this case is no longer a good approximation to the quantum walk described in Sec. 1.1. Note that even in the given range for k, other momentum classes than the neighboring one are involved. Here, the neighboring class is just the dominant partner.

The coin operator, in its general form, is written as a matrix depending on the horizontal and azimuthal angles of a Bloch sphere. Two internal states are mixed by application of the following matrix:

$$\hat{M}(\alpha, \chi) = \begin{pmatrix} cos(\frac{\alpha}{2}) & e^{-i\chi} sin(\frac{\alpha}{2}) \\ -e^{i\chi} sin(\frac{\alpha}{2}) & cos(\frac{\alpha}{2}) \end{pmatrix} \tag{12}$$

This matrix does not posses full SO(2) symmetry, as can be concluded from the diagonal elements. For the purpose of this thesis however, Eq. (12) is sufficient.

As implemented in Ref. [4], $\alpha = \frac{\pi}{2}$ corresponds to a balanced coin, while deviations from this choice return a bias to the walk. For implementing a QKR walk, one would have to apply the mixing and the step operator subsequently to each other.

1.2.4 Light shift phase

As described in detail in Ref. [29], the effective dynamics of the δ-kick behave differently than stated in Sec. 1.2.1. The effective kick dynamics yield $\cos^2$ terms, which may be rewritten in the following [29]:

$$\cos^2(\frac{\theta}{2}) = \frac{1}{2}(\cos(\theta) + 1) \tag{13}$$

This yields the effective Hamiltonian, as experimentally implemented in Ref. [4].

$$\hat{\mathcal{H}} = \frac{1}{2}\hat{p}^2 + k[1 + \cos(\hat{\theta})] \sum_{n=-\infty}^{\infty} \delta(t - n\tau). \tag{14}$$

In consequence the kick operator $\hat{\mathcal{U}}_k$ changes.

$$\hat{\mathcal{U}}_k = e^{-ik(1+\cos(\hat{\theta})\sigma_z)} \tag{15}$$

$$= \begin{pmatrix} e^{-ik} & 0 \\ 0 & e^{ik} \end{pmatrix} \begin{pmatrix} e^{-ik\cos(\theta)} & 0 \\ 0 & e^{ik\cos(\theta)} \end{pmatrix} \tag{16}$$

This additionally introduced „light shift operator“ contributes as a phase difference of $2k$ between the internal states. If the implementation of a QKR-walk is intended, this additional operator leaves a bias on the system and thus has to be compensated. The light shift phase compensation has been attempted in Ref. [4] by introducing a compensation phase ϕ_c within the coin operator $\hat{M}$.

$$\hat{M}(\alpha, \chi) \rightarrow \hat{M}(\alpha, \chi + \phi_c) \tag{17}$$

Please note that this compensation can only succeed partially since the off-diagonal elements can not fully counteract the on-diagonal elements of the light shift operator $e^{-ik\sigma_z}$.

1.2.5 Quantum ratchet

A ratchet is a system in which spatial symmetry is broken. Imagine for example a saw-tooth ratchet from an ordinary toolbox that allows for rotation in one direction and blocks rotation in the other one. Here the symmetry breaking comes from the overarching system itself.

Since our overarching system is the QKR, breaking the symmetry does not come from the potential itself. For our quantum ratchet, the symmetry break lies within the initial state itself. A comprehensive overview of quantum ratchets as used here can be found in Ref. [31, 32].
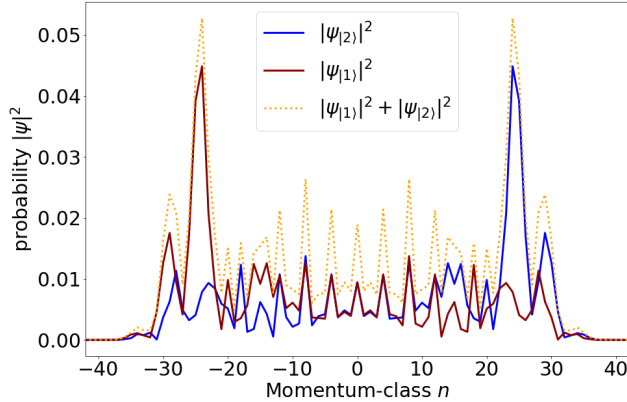
Figure 2: The figure shows the quantum kicked rotor walk, implemented for a ratchet state $\psi_{in} = \frac{1}{\sqrt{5}}|2\rangle \otimes \sum_{n=-2}^{2} e^{is\pi/2}|n\rangle$ in momentum space. The walk is initialized by the $\hat{H}$-gate and then evolved under the $\hat{Y}$-coin. It is shown after $j = 40$ steps in the evolution and $k = 1.45$. It is demonstrated that the internal states evolve in opposite directions of the walk space.

The quantum ratchet consists of at least two initial momentum classes, which have a relative phase shift of $e^{i\pi/2}$ to each other.

$$|\psi_{in}\rangle = \frac{1}{\sqrt{S}} \sum_s e^{is\pi/2}|n = s\rangle. \tag{18}$$

These states can be realized by the application of Bragg pulses [33]. In Ref. [31], the gradient of the kick potential is considered to be the driving force of the system. The strongest gradient and thus the strongest net force is derived at the flanks of the kick potential. The shift of $e^{i\pi/2}$ in the quantum ratchet from Eq. (18) has the purpose to peak the wave function at the flank of the kick potential. Thus, the system experiences a rather directed kick and continues to evolve asymmetrically, as experimentally demonstrated in Ref. [31, 32]. If this concept is applied to QKR-walks from Sec. 1.2.3, the respective internal states experience a kick into opposite directions. That is why also the internal states evolve predominantly in opposite directions.

2 Theoretical background on double quantum kicked rotor

2.1 Topology in quantum walks

In advance of double quantum kicked rotor (DQKR) dynamics, a brief introduction to several ideas regarding topological aspects of quantum walk systems will be given. For a detailed introduction of topological phenomena in quantum walks, consult Ref. [34]. Also, read Ref. [5, 28] for a more detailed introduction to the topological properties of the DQKR system.

Within topology, two bodies are sorted to the same topological class if there exists a continuous transformation that translates from one body to the other, without need for „gluing" or „cutting". Arbitrary deformations to the body are allowed, as long these restrictions are retained. Usually, from the perspective of figures and shapes, the topological class of a body can be identified by its number of holes. In our case, the "bodies" of interest are gapped Hamiltonians. Such a gapped Hamiltonian displays an energy gap between the ground state (zero energy state) and the first excited state within its energy spectrum. The region in between these energy eigenvalues is called „gap". Similar to topology, two gapped Hamiltonians could be in the same topological class if there were a continuous transformation that connects them, while maintaining the zero energy gap. Furthermore, symmetries of the system play an important role in its topological classification, since they will be a precondition to define topological numbers. In our case, the symmetry of interest will be the so-called chiral symmetry.

$$\hat{\Gamma}^\dagger \hat{\mathcal{H}} \hat{\Gamma} = -\hat{\mathcal{H}} \tag{19}$$

9

We will choose $\hat{\Gamma} = \mathbf{1} \otimes \sigma_z$. As demonstrated in Ref. [28, 34], Eq. (19) implies an energy spectrum that is symmetric around zero. Thus every eigenstate can be assigned a chiral symmetric partner with the energy of the opposite sign. In that sense zero energy eigenstates are a special case since they already are their own chiral symmetric partner. Furthermore, we need to define requirements for the transformations we permit as connection between equivalent Hamiltonians, similar to restrictions on transformations allowed in topology.

As might be guessed from the context of topology, the transformations allowed are supposed to be continuous. Similar to forbidding gluing and cutting, we will demand two additional conditions, such as the conservation of the energy gap and the conservation of the symmetries of the system. Here the notion is of chiral symmetry. If all three conditions are fulfilled, the transformation is called adiabatic and the Hamiltonians connected by this transformation are considered to be topologically equivalent. Similar to the number of holes, one can classify topologically equivalent Hamiltonians by their topological invariant.

2.2 Winding number

For chiral symmetric Hamiltonian that also possesses an external degree of freedom with translational symmetry, a quantity called "winding number" is able to capture the topological properties of the system. Let us assume the Hamiltonian at hand is chiral symmetric under $\hat{\Gamma} = \mathbf{1} \otimes \sigma_z$ and has a 2π periodicity in 1D position space. As discussed in Sec. 1.2.2, Boch´s theorem guarantees a lattice structure in momentum space. The 2π-periodicity of the Hamiltonian in position space also implies 2π-periodicity for the energy spectrum. As shown in Ref. [28], the chiral symmetry allows rewriting the Hamiltonian.

$$\hat{\mathcal{H}} = \hat{\mathcal{H}}_{ext} \otimes \hat{\mathcal{H}}_{int} = \begin{pmatrix} 0 & \mathcal{H}(x) \\ \mathcal{H}^*(x) & 0 \end{pmatrix} = E(x)\vec{n}(x) \cdot \vec{\sigma} \tag{20}$$

There it is explained that $\hat{\mathcal{H}}$ can not be dependent on the components of $\hat{\Gamma}$, since it has to fulfill the chiral symmetry condition. Therefore the third component from the vector of Pauli-matrices must not contribute and thus $\vec{n}(x) = (n_1(x), n_2(x), 0)$. Note that the chiral symmetry confines $\vec{n}$ to a plane.
Due to periodicity in local space by the Hamiltonian, both the symmetric energy spectrum $\pm E$ and $\vec{n}$ are periodic in local space as well. Consequently, the winding number can be mathematically defined. As long the energy gap around zero is respected and the chiral symmetry is not violated, the winding number is a well-defined topological invariant. The winding number is defined for the trajectory of $\vec{n}$, within one period. It is computed by solving the following integral:

$$\nu = \int_0^{2\pi} \frac{dx}{2\pi} \left(\vec{n} \times \frac{\partial \vec{n}(x)}{\partial x} \right)_3 \tag{21}$$

Only the third component is considered due to the geometry of the cross product in combination with the confinement of $\vec{n}$ to the plane. Consult Ref. [28] for illustration.

2.3 Periodically driven systems

For periodically driven systems one has to analyze the so-called effective Hamiltonian $\hat{\mathcal{H}}_{eff}$ to discuss the topological properties of the system. Therefore one rewrites the one-period Floquet operator.

$$\hat{\mathcal{U}} = exp\left(-i\hat{\mathcal{H}}_{eff} \cdot \tau\right) \tag{22}$$

Here τ denotes the duration of one period in the evolution. Of special interest will be systems that are periodically driven in time. For such systems, the Floquet operator can be decomposed into its eigenstates $|n\rangle$ with eigenvalues ϵ_n.

$$\hat{\mathcal{U}} = \sum_n = e^{-i\epsilon_n} |n\rangle\langle n| \tag{23}$$

From here it becomes clear that these „quasienergies" are restricted to what can be understood as Brillouin zone $\epsilon_n \in [-\pi, \pi)$. As shown in Ref. [28], these new edge states at $\pm\pi$ are, just like the zero energy states, their own chiral symmetric partners.
For many aspects of quantum mechanics, the energy spectrum is already sufficient to discuss the relevant

physics. Within the context of topology that is not correct. The quasienergy spectrum is unaffected by the choice of the time frame for the Floquet operator since all time frames are equivalent by unitary transformation. However winding number from Eq. (21) is only well defined for chiral symmetric operators. Let $\hat{\mathcal{U}}_1 = exp(\hat{\mathcal{H}}_1)$ and $\hat{\mathcal{U}}_2 = exp(\hat{\mathcal{H}}_2)$ be chiral symmetric. Ref. [28] presents, that if it is possible to rewrite the Floquet operator.

$$\hat{\mathcal{U}} = \hat{\mathcal{U}}_1 \cdot \hat{\mathcal{U}}_2 \cdot \hat{\mathcal{U}}_1 \tag{24}$$

Then $\hat{\mathcal{U}}$ is chiral symmetric. In other words, the time frame must be symmetric under time inversion.

2.4 Topological phase transitions

If a chiral symmetric one cycle Floquet operator like in Eq. (22) is found and its symmetry and the energy band gap are respected, then as described in Sec. 2.1, the topological winding number is contained. Let us turn around this line of thought and assume that the operator stays chiral symmetric under the transformations that are taken. Since the operator stays chiral symmetric, the topological number ν can only change if the bandgap closes. As illustrated in Ref. [34], the bandgap can only close at the previously discussed special cases $E = 0$ and $E = \pi$.

Consider the following analogy on topology for some further intuition: For a moment understand the energy band gap as separation in space between two bodies, such as e.g. two tori, and count the total number of holes in the system as the topological number. Now apply continuous transformations that forbid gluing or cutting. The topological number is contained, as long the separation of the bodies is contained. If the bodies touch, the topological number may change. In that analogy, the bands can roughly be understood as the two geometrical figures and the winding number as the topological number that may only change if the gap closes. How the winding number changes in detail depends, similar like in the analogy, on the specifics of the transformation.

2.5 Double quantum kicked rotor

The double quantum kicked rotor is a quantum system with an internal spinor degree of freedom, kicked twice in one period. Similar to the QKR from Sec. 1.2.1 the kicks appear periodically for an infinitely short time and come with different kick strengths k_1 and k_2. In between the kicks, the system undergoes a free evolution. Its topological properties are discussed in Ref. [5]. The system Hamiltonian reads

$$\hat{\mathcal{H}} = \frac{\hat{p}^2 \otimes \mathbf{1}}{2} + k_1 \cos(\hat{\theta}) \otimes \hat{\sigma}_x \cdot \sum_{n=0}^{\infty} \delta(t - 2n\tau) + k_2 \sin(\hat{\theta}) \otimes \hat{\sigma}_y \cdot \sum_{n=0}^{\infty} \delta(t - (2n+1)\tau). \tag{25}$$

The Floquet operator can be derived. Again a choice of parameters $\tau = 4\pi$ returns the resonant step operator:

$$\hat{\mathcal{U}}_{step} = e^{-i\frac{\hat{p}^2}{2}\tau} e^{-ik_2\sin(\hat{\theta})\sigma_y} e^{-i\frac{\hat{p}^2}{2}\tau} e^{-ik_1\cos(\hat{\theta})\sigma_x}$$
$$\stackrel{\tau=4\pi}{=} e^{-ik_2\sin(\hat{\theta})\sigma_y} e^{-ik_1\cos(\hat{\theta})\sigma_x}. \tag{26}$$

Note that the Hamiltonian has no dependency on σ_z, as demanded in Sec. 2.2 as condition for chiral symmetry. The demand on time inversion symmetry from Sec. 2.3 allows for only two possible time frames:

$$\hat{U}_1 = e^{-i\frac{k_1}{2}\cos(\hat{\theta})\sigma_x} e^{-ik_2\sin(\hat{\theta})\sigma_y} e^{-i\frac{k_1}{2}\cos(\hat{\theta})\sigma_x} \tag{27}$$

$$\hat{U}_2 = e^{-i\frac{k_2}{2}\sin(\hat{\theta})\sigma_y} e^{-ik_1\cos(\hat{\theta})\sigma_x} e^{-i\frac{k_2}{2}\sin(\hat{\theta})\sigma_y}. \tag{28}$$

As proven in Ref. [28], $\hat{\mathcal{H}}_1 \equiv k_1\cos(\hat{\theta})\sigma_x$ and $\hat{\mathcal{H}}_1 \equiv k_2\sin(\hat{\theta})\sigma_y$ are both chiral symmetric and thus also Eq. (27) (28) are chiral symmetric, as stated in Sec. 2.3. To extract the topological properties, these operators have to be rewritten into the following form:

$$\hat{U}_i = \sum_{\theta} e^{-iE(\theta)\vec{n}_i\vec{\sigma}} \tag{29}$$

As presented in Ref. [5, 28], this succeeds with:

$$E(\theta) = \arccos(\cos(K_1)\cos(K_2)) \tag{30}$$

$$n_{1,x} = \frac{\sin(K_1)\cos(K_2)}{\sin(E)} \qquad\qquad n_{1,y} = \frac{\sin(K_2)}{\sin(E)} \tag{31}$$

$$n_{2,x} = \frac{\sin(K_1)}{\sin(E)} \qquad\qquad n_{2,y} = \frac{\sin(K_2)\cos(K_1)}{\sin(E)} \tag{32}$$

With $K_1 = k_1\cos(\theta)$ and $K_2 = k_2\sin(\theta)$. Remember that the third component of $\vec{n}$ vanishes as explained in Sec. 2.2 due to chiral symmetry. With Eq. (21) and the equations above, the topological winding number can be computed. A phase diagram in dependency of k_1 and k_2 is shown in Ref. [5]. As hinted in Sec. 2.4, the energy band gap only closes for $E = 0$ and $E = \pi$. This leaves us with the condition for a topological phase transition of $\cos(K_1)\cos(K_2) \overset{!}{=} \pm 1$.

2.6 Mean chiral displacement

Since the winding number is not an experimentally accessible observable a quantity that is connected to it, called the mean chiral displacement (MCD), will be introduced. For the MCD the momentum distributions of the two internal states evolved under the chiral symmetric evolution operators $\hat{U}_1$ and $\hat{U}_2$ are measured. From this, the momentum expectation values for the internal states can be computed. The MCD describes the difference between these two numbers.

$$\begin{aligned} C_l(t) &= \langle\psi_t|\hat{n}\otimes-\sigma_z|\psi_t\rangle \\ &\equiv \langle\psi_0|\hat{U}_l^{-t}(\hat{n}\otimes-\sigma_z)\hat{U}_l^t|\psi_0\rangle \end{aligned} \tag{33}$$

In Ref. [5] a theorem is discussed, that connects this measurable quantity with the topological winding number.

$$\bar{C}_l(t) = \frac{1}{t}\sum_{\tilde{t}=1}^{t} C_l(\tilde{t}) \xrightarrow{t\gg 1} \frac{\nu_l}{2} \tag{34}$$

In Ref. [6] it has already been tested that this convergence becomes very good for an average over $T = 10$ applications of the evolution operator. Also, it is stated that already for $T = 5$ steps a good signal can be seen.
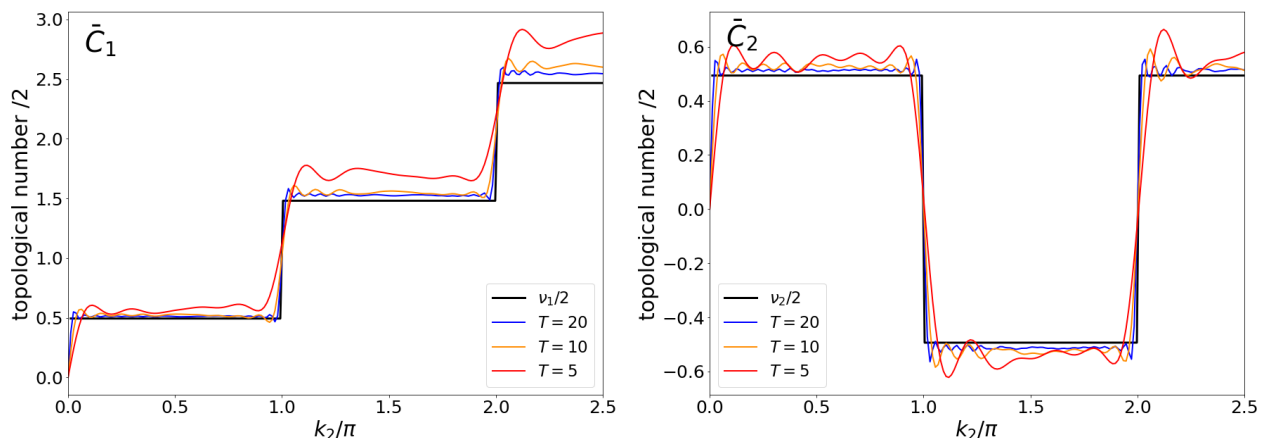

Figure 3: Illustrated is the convergence of the time-averaged MCD for the chiral symmetric evolution operators $\hat{U}_1$ and $\hat{U}_2$. The theoretical curves calculated by Eq. (21) are represented in black. For five applications of the evolution operator, the steps are already quite well visible. A stronger convergence is achieved at higher time steps.

3 Reinterpretation of experimentally realized momentum space quantum walk

3.1 Experimental framework

Recently in Ref. [4], a discrete-time quantum walk has been realized in momentum space by utilization of a Bose-Einstein condensate (BEC). The walk demonstrated has been stable for roughly up to fifteen steps in the evolution. It was reasonably well in line with theoretical predictions, but also displayed behavior deviating from the previous analysis. The original interpretation of these discrepancies is presented in Ref. [3] and assumed a thermal cloud of atoms that do not respond to the quantum ratchet. A reinterpretation has been found, for the experimental effects deviating from the original theoretical prediction to be a result of the choice of the initial state. Especially this new explanation does not rely on effects beyond the setup of the experiment.

The underlying system to the experiment performed in Ref. [4] is the quantum kicked rotor from Sec. 1.2. The internal states of the BEC of ^{37}Rb atoms addressed by the protocol are the two Zeeman hyperfine levels $F = 1$, $m_F = 0$ and $F = 2$, $m_F = 0$. This choice yields effectively an internal spinor degree of freedom. The δ-pulses from the kick operator are experimentally realized by turning an optical pulsed lattice on and off. The optical lattice supplied a kick strength of $k = 1.45$. By the detuning of the laser the internal states experience respectively either positive or negative kick strength. The time in between two consecutive pulses is chosen to be $\tau = 4\pi$, resolving in the resonant step operator from Eq. (6). The choice of ordering the basis rewrites the kick operator in the following manner:

$$\hat{\mathcal{U}}_k = |1\rangle\langle 1|e^{ik\cos(\hat{\theta})} + |2\rangle\langle 2|e^{-ik\cos(\hat{\theta})}. \tag{35}$$

The initial state chosen for the experiment is a ratchet state from Sec. 1.2.5. This state was generated by a Bragg pulse and consisted of two initially involved momentum classes, $|\psi_{in}\rangle = |1\rangle \otimes \frac{1}{\sqrt{2}}(|n = 0\rangle + i|n = 1\rangle)$. The coin operator has been realized by the application of resonant microwave (MW) radiation, mixing the internal states. Its implementation takes place during the free evolution. With α and χ being horizontal and azimuthal angles on a Bloch sphere, the MW application is mathematically described by Eq. (12). In Ref. [3, 4] the implemented experimental protocol is described. Similar to the protocols discussed in Sec.1.1, the sequence implements the Hadamard-coin $\hat{H}_1 = \hat{M}(\frac{\pi}{2}, \pi)$ as a gate. Afterwards the walk is evolved by the beamsplitter matrix $\hat{Y} = \hat{M}(\frac{\pi}{2}, -\frac{\pi}{2})$. This way the initial state is applied to the full evolution operator for j time steps $(\hat{U}_{\text{step}})^j = [\hat{T}\hat{Y}]^j[\hat{T}\hat{H}]$. Finally, the momentum distribution is measured for both internal states in dependency of the number of steps, as $P(n, j) = P_{|1\rangle}(n, j) + P_{|2\rangle}(n, j)$. If this walk is numerically implemented, as shown in Ref. [3], one finds a walk that does quickly evolve away from its origin position. Yet, the experiment observed a significant part of the wave function that does not at all evolve far away from its initially occupied momentum classes. This is the experimental deviation from the theory, mentioned above. As already hinted, this behavior was originally explained by a thermal cloud of atoms, not responding to the ratchet and thus not evolving far away from their initial position in momentum space. An alternative theory for the observed behavior is presented below.

3.2 Alternate protocol

As already mentioned in Sec. 1.2.4, reformulating the $\cos^2$ terms yields an additional term within the expression for the kick operator. For the two-state system at hand, the kick operator is given by Eq. (16). The additional phase difference of $2k$ coming along with each kick would result in a deviation from the intended QKR walk. All coin operators in the intended protocol are balanced ($\alpha = \pi/2$) and thus the walk is expected to evolve symmetrically. To compensate for the light shift effect, the phase χ within the MW-pulses is chosen to produce a symmetrically evolving walk. Therefore the second argument of $\hat{M}$ is only indirectly known, by the knowledge that the MW in combination with the light shift part of the kick operator is supposed to combine for a balanced operator. Due to the limited access of knowledge to the phase, χ one might suggest that effectively a different protocol has been implemented. A possibility of this idea would be $(\hat{U}_{\text{step}})^j = [\hat{T}\hat{H}]^j[\hat{T}\hat{Y}]$, since both $\hat{H}$ and $\hat{Y}$ are balanced coins. This line of thought is supported if one looks

at the combined effect of the light shift phase and coin matrix with yet unknown phase.

$$\hat{M}(\frac{\pi}{2}, \chi)e^{-ik\hat{\sigma}_z} = \frac{1}{\sqrt{2}} \begin{pmatrix} 1 & e^{-i\chi} \\ -e^{i\chi} & 1 \end{pmatrix} \begin{pmatrix} e^{-ik} & 0 \\ 0 & e^{ik} \end{pmatrix}$$

$$= \frac{1}{\sqrt{2}} \begin{pmatrix} e^{-ik} & e^{-i(\chi-k)} \\ -e^{i(\chi-k)} & e^{ik} \end{pmatrix} \tag{36}$$

$$\equiv \frac{1}{\sqrt{2}} \begin{pmatrix} 1 & e^{-i(\chi-2k)} \\ -e^{i\chi} & e^{i2k} \end{pmatrix}$$

Where in the last step a global phase of e^{-ik} has been pulled out. No matter the choice of χ, the light shift effects can not be fully compensated. But experimentally, χ is chosen by finding a balanced coin. A balanced coin can be found by choosing $\chi = 2k = \pi$. This special choice would implement the following coin operator:

$$\hat{H}_2 = \frac{1}{\sqrt{2}} \begin{pmatrix} 1 & 1 \\ 1 & -1 \end{pmatrix} \tag{37}$$

This possibility appears to be rather plausible if one considers that indeed $k = 1.45 \approx \pi/2$. The idea that effectively a different coin might have been implemented is additionally supported by the problem that the precise timing of the internal rotation of the atom is not known. This way the second phase angle in the MW suffers effective fluctuations and thus is effectively not under full experimental control. At this point, it becomes important to point out that the coin in Eq. (37) is an altered version of the Hadamard coin $\hat{M}(\frac{\pi}{2}, \pi) \equiv \hat{H}_1$, originally planned for the gate. In other words, there are two different Hadamard coins, with their difference being that once the -1 lies once on the off-diagonal and once on the diagonal.

$$\hat{H}_1 = \frac{1}{\sqrt{2}} \begin{pmatrix} 1 & 1 \\ -1 & 1 \end{pmatrix} \qquad \hat{H}_2 = \frac{1}{\sqrt{2}} \begin{pmatrix} 1 & 1 \\ 1 & -1 \end{pmatrix}. \tag{38}$$

Both coins have similar features: The upper two entries mix the internal states by addition, the lower two ones by subtraction. Unexpectedly their implementation unveils a distinctively different behavior of the walk, demonstrated in Fig. 4 a). It is seen that the implementation of the alternatively assumed protocol with the use of the $\hat{H}_1$ coin returns the same distribution as the original proposal. If however the $\hat{H}_2$ coin is implemented, we see a significant part of the wave function resting close to the zero momentum class.

3.3 Dependency of dispersion on initial state

The ideal quantum walk discussed shown in Fig. 1 does not display any different behavior between the different walk protocols discussed above. That is due to the properties of its step operator. The ideal step operator shifts the fraction of the wave function occupying a specific momentum class partially to the left and the right. In this way, one can interpret the step operator in a way as it „looks" at a specific momentum class. Then within this specific class, it looks at the fraction of the internal states occupying it and shifts these accordingly. Subsequently it „repeats" this for all the remaining momentum classes. The point of this rather trivial notion is that the ideal shift does not „care" about the relative phase of the states when it executes the shift. So as long the coin is a balanced coin and the same momentum classes are initially occupied, all walks are expected to behave the same. Since when the coin is balanced, the shift operator only sees a 50% portion of each internal state in the respective momentum class. In summary, the observed difference between different walk protocols in Fig. 4 a) must be a relic of the properties of the QKR-system, namely dispersion discussed briefly below.

The initial state at hand is a ratchet state involving two momentum classes. As described in Ref. [31,32] and Sec. 1.2.5, the purpose of the ratchet state is to peak at the flanks of the kick potential in angular momentum space. Considering the gradient of the kick potential to be the driving force, it is strongest at the flanks of the potential. This is utilized by the ratchet state. Since it is designed to center at the flanks of the potential, it experiences the maximum net force the system can provide.

Naturally, we discuss the evolution of wave functions. Thus by the Heisenberg principle, a broader state in momentum space gives a slimmer state in angular momentum space. Consequently adding more momentum classes to the initial ratchet state, the initial wave function will be more densely peaked at the flank of the potential. Thus by involving more momentum classes, the system experiences a more uniform kick strength. This way a broad initial ratchet state in momentum representation decreases dispersive effects.
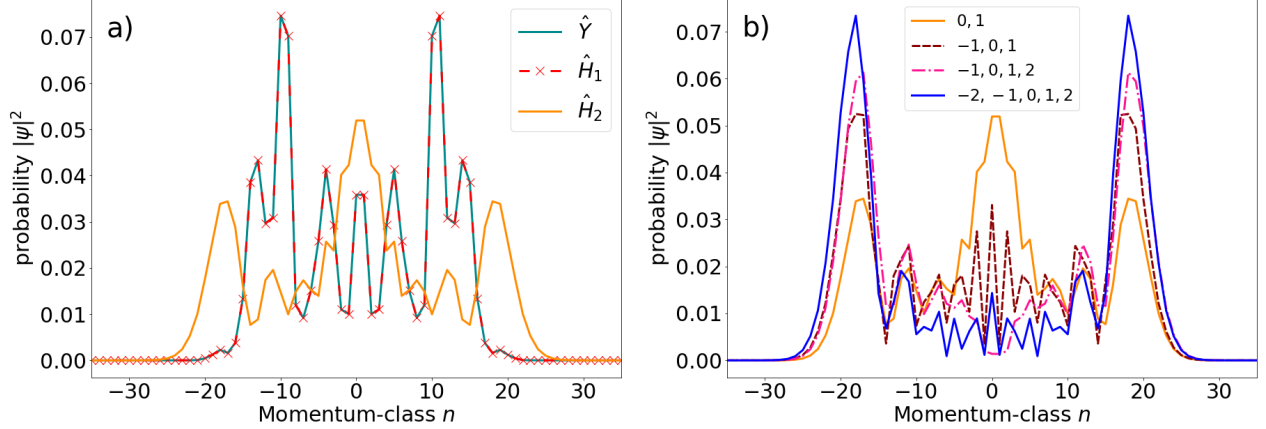
Figure 4: Presented are momentum distributions for QKR walks after $j = 20$ steps in the evolution and $k = 1.45$. Fig. a) presents the momentum distribution for different walk protocols. „$\hat{Y}$" denotes the originally proposed protocol from Sec. 3.1. „$\hat{H}_{1/2}$" use the $\hat{Y}$-coin as gate and then the $\hat{H}_1$ or $\hat{H}_2$ coin for the walk. While the „$\hat{Y}$" and the „$\hat{H}_1$" protocol resolve in the same distribution, the „$\hat{H}_2$" protocol shows significant deviations with a dominant peak in the center of the distribution.

For Fig. b) all the walks are initialized by the $\hat{Y}$-coin and continued by the $\hat{H}_2$-coin, assuming a light shift induced protocol deviating from the original proposal from Ref. [4]. The labels denote the involved momentum classes to the initial ratchet state. The numbers correspond to „s" from Eq. (18). The more momentum classes are included in the initial state, the less dominant becomes the peak in the center region. Remember that the state from Ref. [4] only includes the momentum classes $s = 0$ and $s = 1$.

Also, the choice of the kick strength is not arbitrary. Looking at Sec. 1.2.3, one notes that $k = 1.45$ lies within the interval of kick strengths that produce strong coupling between neighboured momentum classes. As already explained there, also other momentum classes are involved. This is another source for dispersive properties in the system. It is only likely that this origin for dispersion is highlighted for a narrow initial ratchet. As already explained, a ratchet involving fewer momentum classes experiences effectively a rather broad range of significantly contributing kick force from the gradient of the potential. Thus the way the spreading upon the neighboring momentum classes happens should be less uniform across the wave function for a narrow ratchet, resolving in stronger dispersion.

From this line of thought one can draw the following argumentation:

If relatively few momentum classes are involved in the initial ratchet, the state will be rather broad at the flanks of the kick potential. Thus, the system will experience a less uniform force resolving from the kick. That finally highlights the dispersive quantities of the QKR-system.

A final indication for dispersive effects causing the observed behavior may be discussed. In Ref. [30] it has been observed that also for the $\hat{Y}$-protocol at higher kick strength $k \gtrsim 3$ a peak emerges in the center of the distribution. Numerical tests show that for lower values at $k \approx 0.75$ the dominant peak in the center of the $\hat{H}_2$-walk vanishes, even though an initial ratchet with only two involved momentum classes is implemented. Higher values for k imply more dispersion in the system since more momentum classes can be effectively linked by the kick operator. Also, it seems consistent with the originally proposed walk, that at higher k more dispersion induces a peak in the center of the distribution. The present protocol implementing the walk with the $\hat{H}_2$-coin seems to be more sensitive to dispersive effects, displaying a similar behavior already at $k = 1.45$ for a narrow initial ratchet state. An illustration of this behavior is found in A.1.

The experiment involved only two states in the ratchet. As demonstrated in Fig. 4 b), involving already three momentum classes to the initial state reduces the contribution of the center part of the wave function significantly. Here again, the protocol with the $\hat{H}_2$-coin is considered. For an even broader ratchet, the center part almost vanishes completely. In this case, the walk is much closer to the ideal quantum walk, displayed by the predominant sidearms. Consequently, the rather dominant central peak is only observed

under a relatively rare configuration: The walk being implemented by the $\hat{H}_2$-coin and a narrow initial momentum state. The narrow state then highlights the dispersive properties of the system, allowing for more prominent deviations from the ideal quantum walk. Since the experiment used such a narrow state with only two momentum classes, from the perspective of assuming a different walk protocol the walk is expected to demonstrate this dominant non-vanishing part of the wave function in the middle of the distribution.

3.4 Analytical solution

For the originally proposed walk exists an analytical solution for the momentum distribution, computed in Ref. [29]. Following along the original calculation a similar solution can be written down for the present case of a different walk protocol, initialized by the $\hat{Y}$-coin and continued by the $\hat{H}_2$-coin. For solving this walk one has to solve for the evolution U^T after T steps.

$$\hat{U} = \hat{H}_2\hat{K} = \frac{1}{\sqrt{2}} \begin{pmatrix} 1 & 1 \\ 1 & -1 \end{pmatrix} \begin{pmatrix} e^{-ik\cos(\hat{\theta})} & 0 \\ 0 & e^{ik\cos(\hat{\theta})} \end{pmatrix} \tag{39}$$

The initial state is considered to be $|\psi_{in}\rangle = |1\rangle \otimes \frac{1}{\sqrt{S}}\sum_s e^{is\pi/2}|n=s\rangle$. The calculation is done in A.2 for an arbitrary large ratchet state. The solution found is exact, but the calculation itself does not reveal a deeper insight into why exactly the different walk protocols demonstrate the different behavior. The momentum distribution is given in Eq. (40). It satisfies the same expression as in Ref. [29] however, the coefficients are different by a $(-1)^{-l}$ within the sums.

$$
\begin{aligned}
P(n,T) &= P_{|1\rangle}(n,T) + P_{|2\rangle}(n,T) \\
&= \frac{1}{2^{T+1}S}\left[\left(\sum_{l=0}^{N}\sum_s a_{l,1}(-1)^s J_{(n-s)}\left((N-2l-1)k\right)\right)^2 + \left(\sum_{l=0}^{N}\sum_s a_{l,2}(-1)^s J_{(n-s)}\left((N-2l+1)k\right)\right)^2 \right. \\
&\left. + \left(\sum_{l=0}^{N}\sum_s a_{l,1}(-1)^s J_{(n-s)}\left(-(N-2l-1)k\right)\right)^2 + \left(\sum_{l=0}^{N}\sum_s a_{l,2}(-1)^s J_{(n-s)}\left(-(N-2l+1)k\right)\right)^2 \right]
\end{aligned}
\tag{40}
$$

Here $J_\alpha(x)$ are Bessel functions of the first kind and $N \equiv T - 1$. The coefficients $a_{l,1/2}$ are given by:

$$
\begin{aligned}
a_{l,1} &= \frac{1}{2^N}\sum_{j=0}^{N/2}\sum_{m=0}^{l}\left(\binom{N}{2j} - \binom{N}{2j+1}\right)\binom{j}{m}\binom{N-2m}{l-m}(-1)^{N-l+m}\cdot 8^m \\
&+ \frac{1}{2^N}2\sum_{j=0}^{N/2}\sum_{m=0}^{l-1}\binom{N}{2j+1}\binom{j}{m}\binom{N-2m-1}{l-m-1}(-1)^{N-l+m}\cdot 8^m \\
&- \frac{1}{2^N}2\sum_{j=0}^{N/2}\sum_{m=0}^{l}\binom{N}{2j+1}\binom{j}{m}\binom{N-2m-1}{l-m}(-1)^{N-l+m}\cdot 8^m.
\end{aligned}
\tag{41}
$$

$$a_{l,2} = \frac{1}{2^N}\sum_{j=0}^{N/2}\sum_{m=0}^{l}\binom{N+1}{2j+1}\binom{j}{m}\binom{N-2m}{l-m}(-1)^{-l+m}\cdot 8^m. \tag{42}$$

Even though no deeper conclusion can be drawn, it is not too surprising that different coefficients lead up to a different shape of the final momentum distribution. Since interference phenomena are discussed, the walk is quite susceptible to changes within the way the Bessel functions are weighted in the sums. The „laziness" of the walk, meaning that there is a certain probability not to change the momentum class after a kick, is reflected in the walk being described by Bessel functions since those have generally a non-vanishing probability at $J_\alpha(x=0)$. Note that Eq. (40) reflects the expected dependence on the number of time steps and the number of included momentum classes to the initial ratchet state.
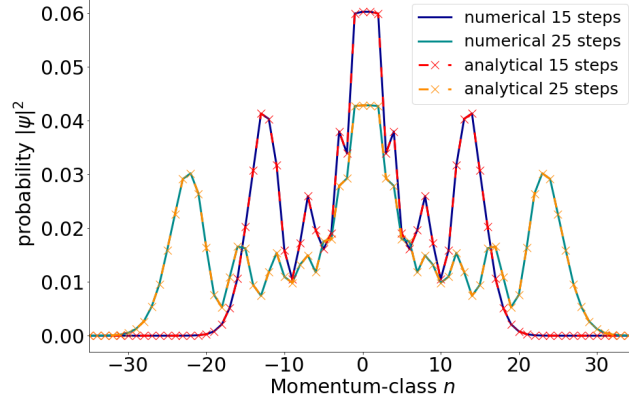
Figure 5: Shown are momentum distributions at two different time points in the evolution. Compared are the numerical simulations and the analytical solution from Eq. (40). It is demonstrated that the solution is exact since no deviations from the simulation can be found.

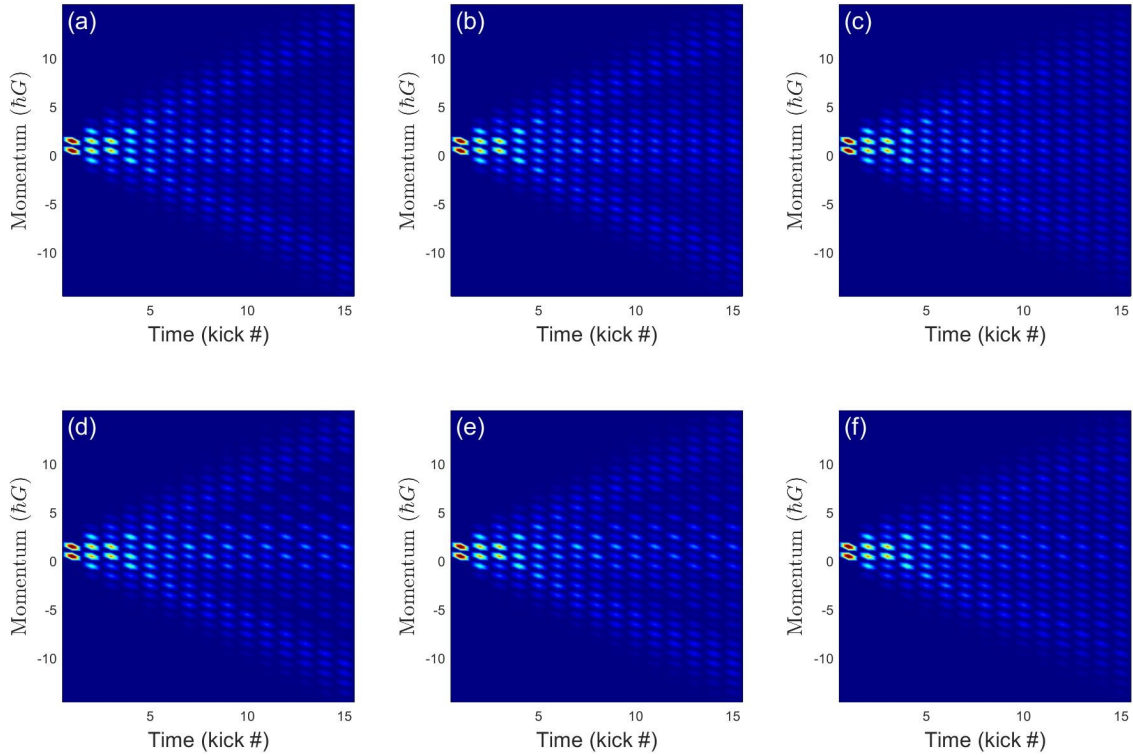## 3.5   Comparison between competing theoretical explanations

Figure 6: Shown are two walk protocols implemented at $k = 1.45$, alternating from the original proposal. The plots in the upper row show the alternate walk protocol, using the $\hat{Y}$-coin as gate and the $\hat{H}_2$ coin to evolve the walk. The walks from the lower row are also implemented with the $\hat{Y}$-coin but then evolved by the light shift induced coin from Eq. (36) with $\chi = \pi$. Both slightly different coins share the same characteristics, such as linearly evolving sidearms and a significant part in the distribution not evolving at all. From left to right quasimomentum is increased. Image a) and d) correspond to the ideal case $\beta_{FWHM} = 0\hbar G$, b) and e) correspond to $\beta_{FWHM} = 0.01\hbar G$ and finally c) and f) are implemented with $\beta_{FWHM} = 0.025\hbar G$. The images are created by an average over 1000 realizations.

All thoughts so far did not yet consider a finite quasimomentum distribution. Due to finite temperature, this does not satisfy the experimental condition. Consequently for $\beta \neq 0$ the free evolution operator deviates from resonant configuration, resolving in an operator that deviates from unity. Since the MW is applied to the system during the free evolution, the requirement for re-including the free evolution in the simulation protocol is met in the following way:

$$\hat{M}(\alpha, \chi) \rightarrow e^{-i\frac{(\hat{n}+\beta)^2}{2}\tau}\hat{M}(\alpha, \chi) \tag{43}$$

To reflect the experimental setup from Ref. [4] in the simulations, the duration of the MW application is taken to be $\tau = 4\pi$ and β is drawn from a Gaussian distribution of certain width. More physically accurate would be a Thomas-Fermi distribution, yet Gaussian random numbers are numerically easily accessible and also satisfying for our purpose. The impact of quasimomentum distribution of finite width β_{FWHM} is shown in Fig. 6.

Here two slightly different walks are compared to each other. Once, the implementation with $\hat{Y}$-gate and $\hat{H}_2$-coin for the walk and in the other case the walk is implements Eq. (36) at $\chi = \pi$ and $k = 1.45$ as coin. Both protocols are suspected to be effectively closer to what has been experimentally implemented. Fundamentally, they show the same characteristics. Such as a dominant non-vanishing part in the center of the distribution and sidearms evolving linearly in momentum space. These characteristics stay even visible for higher quasimomentum but become less distinct. In Ref. [4] a quasimomentum distribution of $\beta_{FWHM} = 0.025\hbar G$ is reported. This value is taken by an indirect measurement and thus not precisely known. This is to point out since the differentiation between the sidearms and the center region, within the simulations of Fig. 6, is already less distinct at $\beta_{FWHM} = 0.025\hbar G$ than within the experimental data shown for comparison in Fig. 7. This detail resolves if the width of the quasimomentum distribution had been overestimated.

Yet it is also to point out that the experimental data shows exactly the discussed characteristics from above, meaning a dominant central region and linearly evolving sidearms. The central area is not at all predicted in the originally proposed walk shown in Fig. 7 d). This had been fixed in Ref. [3], shown in Fig. 7 b), by proposing the already mentioned thermal cloud of atoms. However, in this explanation, the shape of the sidearms stays the same and reminds more of a „fish-bone structure" instead of the experimentally observed linear shape.

Both characteristics follow as a natural consequence if one assumes that effectively the alternative protocol, as suggested in Sec. 3.2, had been implemented. Even though the central region were successfully explained by a different theory, additional physical effects beyond the basic experimental setup had to be introduced. Within the theory presented in this thesis, the observed behavior of the walk follows from less assumptions. Above in Fig. 4, strong predictions have been made regarding the fraction of the central region in the distribution, in dependency of the number of momentum classes included in the initial ratchet. This opens the door for testing the correctness of the reinterpretation for the experiment, since the thermal cloud would be expected to appear independently of the size of the ratchet. Imagining the experiment would be repeated with at least three initial momentum classes, and the fraction of the wave function that was observed would or would not change accordingly, one could discriminate for one of the theories.
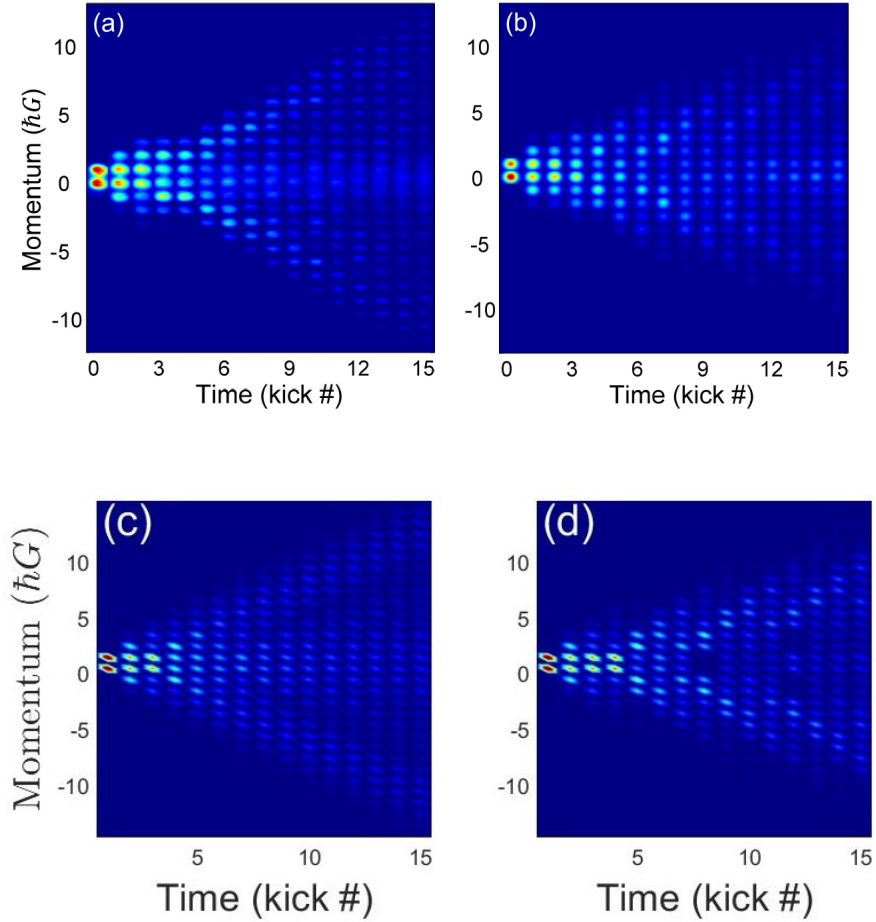
Figure 7: Quantum kicked rotor walks realized with $k = 1.45$. Image a) and b) are taken with kind permission of the authors from Ref. [3] for reasons of comparison. Image a) shows the experimental data and b) shows the theoretical explanation, assuming the proposed protocol and introducing a thermal cloud of atoms that do not respond to the ratchet. Image c) and d) are created in the course of this work. They show walks that are numerically simulated at $\beta_{FWHM} = 0.01\hbar G$. While c) presents the alternate protocol with $\hat{Y}$-coin as gate and $\hat{H}_2$-coin for the walk, d) presents the walk with $\hat{H}_2$-coin as gate and $\hat{Y}$-coin for the walk. So c) is the alternatively suggested protocol from Sec. 3.2 and d) corresponds to the originally assumed protocol. The previous theory in b) can explain the central area in the distribution. Still, the linear expansion of the sidearms is described more clearly by c), assuming a light shift induced alternative protocol.

4 Possibilities for experimental implementation of Floquet topological phases

In Ref. [5], possibilities for experimental measurement of the topological phases within the DQKR system from Sec. 2.5 have been discussed. Similar to the quantum walk experiment from Ref. [4], a BEC would be evolved in momentum space. Here, the system would be evolved under the chiral symmetric operators $\hat{U}_1$ and $\hat{U}_2$. The winding number would be measured by the mean chiral displacement from Sec. 2.6 in dependency of k_2. As stated above, there are two time-frames in the system that satisfy the required symmetries, so that topological winding is a well-defined quantity. To implement the operators with the setup from Ref [4], using the kick and MW operators from Sec. 1.2.3, $\hat{U}_1$ and $\hat{U}_2$ are rewritten as already suggested in Ref. [5, 6, 28]. Here, since the setup from Ref [4] is only able to supply σ_z kicks but not the required σ_x or σ_y kicks, the system is „rotated " by MWs into the correct orientation and then experiences a kick by an optical pulsed lattice, as in the quantum walk experiment.

$$
\begin{aligned}
\hat{U}_1 =& \; e^{-i\frac{k_1}{2}\cos(\hat{\theta})\sigma_x} e^{-ik_2\sin(\hat{\theta})\sigma_y} e^{-i\frac{k_1}{2}\cos(\hat{\theta})\sigma_x} \\
=& \; \hat{M}(-\frac{\pi}{2},0)K_1^{\frac{1}{2}}\hat{M}(\frac{\pi}{2},0)\hat{M}(-\frac{\pi}{2},\frac{\pi}{2})K_2\hat{M}(\frac{\pi}{2},\frac{\pi}{2})\hat{M}(-\frac{\pi}{2},0)K_1^{\frac{1}{2}}\hat{M}(\frac{\pi}{2},0)
\end{aligned}
\tag{44}
$$

$$
\begin{aligned}
\hat{U}_2 =& \; e^{-i\frac{k_2}{2}\sin(\hat{\theta})\sigma_y} e^{-ik_1\cos(\hat{\theta})\sigma_x} e^{-i\frac{k_2}{2}\sin(\hat{\theta})\sigma_y} \\
=& \; \hat{M}(-\frac{\pi}{2},\frac{\pi}{2})K_2^{\frac{1}{2}}\hat{M}(\frac{\pi}{2},\frac{\pi}{2})\hat{M}(-\frac{\pi}{2},0)K_1\hat{M}(\frac{\pi}{2},0)\hat{M}(-\frac{\pi}{2},\frac{\pi}{2})K_2^{\frac{1}{2}}\hat{M}(\frac{\pi}{2},\frac{\pi}{2})
\end{aligned}
\tag{45}
$$

$$
\hat{K}_1 = e^{-ik_1\cos(\hat{\theta})\sigma_z} \tag{46}
$$

$$
\hat{K}_2 = e^{-ik_2\sin(\hat{\theta})\sigma_z} \tag{47}
$$

$$
\hat{K}_{1,2}^{1/2} \equiv \hat{K}_{1,2}(\frac{k}{2},\theta) \tag{48}
$$

The operator $\hat{M}$ is the same as before from Eq. (12). Since there has been an error in sign along with the calculations in Ref. [6, 28], rewriting the operators is presented again in B.1 to avoid further confusion. The impact of lattice vibrations upon the stability of the topological phases was already investigated in Ref. [6] and was found to have a rather weak impact.

The rewritten operators from above leave us with two problems not yet considered. The microwaves have to be applied for a certain amount of time to fully rotate the system and produce a strong signal. Like before this condition is included by Eq. (43).

Another complication is that the evolution operator shows a large amount of MW rotations. Within an experimental implementation complications like atom loss of the BEC or decoherence are expected to faint the signal significantly, if the experimental duration becomes too long. The fainting of signal over time is already seen in Fig. 7 a). Imagining every MW would be applied for a full Talbot period $\tau = 4\pi$, like in Ref. [4] to satisfy the resonance condition, the demand on many MW applications here would pose a problem to measure the MCD for a sufficient amount of applications of $\hat{U}_{1,2}$.

It has been reported [35] that experimentally the shortest realizable MW ontime to still produce a good signal lies close to a quarter of the Talbot time. If chosen exactly a quarter Talbot time, $\tau = \pi$ in our units, a new resonance condition can be formulated. Remembering that the free evolution operator only becomes unity by choosing $\tau = 4\pi$ and neglecting quasimomentum, it is not obvious that a shorter ontime of the MW will actually implement a resonant protocol, without the phase from the free evolution operator disturbing the system to a degree that topological winding would not be measurable anymore. Indeed, if we would apply the operators $\hat{U}_{1,2}$ in their form presented in Eq. (44), (45) for t times with a MW duration of $\tau = \pi$, the protocol turns out to behave anti-resonant, as will be investigated below.

In other words: The free evolution of the system during the MW application poses a problem that we intend to encounter by holding the MW ontime rather short. It will turn out, that this will demand a modified protocol for the implementation of $\hat{U}_{1,2}$. This modification will turn out to save MW rotations, which will additionally simplify the experiment.

4.1 Antiresonant protocol

Some preparations for proving the protocol being resonant or antiresonant respectively are shown in B.2, using similar identities for the free evolution operator then in Ref. [28]. The bottom line is that the free evolution operator, by neglecting quasimomomentum, can be identified with the shift operator in local space: $\hat{P}^2(\beta = 0, \tau = \pi) = \hat{T}(\pi)$. For all further analytical considerations we focus on the case $\hat{P}(\beta = 0, \tau = \pi) \equiv \hat{P}_\pi$. Furthermore the evolution of the quantum system is considered as a Floquet problem, meaning that the full evolution operator is given by applying the one cycle evolution operator just t times.

$$\hat{U}_1^t = \left[\hat{M}(-\frac{\pi}{2}, 0)\hat{K}_1^{\frac{1}{2}}\hat{M}(\frac{\pi}{2}, 0)\hat{M}(-\frac{\pi}{2}, \frac{\pi}{2})\hat{K}_2\hat{M}(\frac{\pi}{2}, \frac{\pi}{2})\hat{M}(-\frac{\pi}{2}, 0)\hat{K}_1^{\frac{1}{2}}\hat{M}(\frac{\pi}{2}, 0) \right]^t \tag{49}$$

$$\hat{U}_2^t = \left[\hat{M}(-\frac{\pi}{2}, \frac{\pi}{2})\hat{K}_2^{\frac{1}{2}}\hat{M}(\frac{\pi}{2}, \frac{\pi}{2})\hat{M}(-\frac{\pi}{2}, 0)\hat{K}_1\hat{M}(\frac{\pi}{2}, 0)\hat{M}(-\frac{\pi}{2}, \frac{\pi}{2})\hat{K}_2^{\frac{1}{2}}\hat{M}(\frac{\pi}{2}, \frac{\pi}{2}) \right]^t \tag{50}$$

In order to introduce a finite MW-ontime of $\tau = \pi$ one substitutes as stated above $\hat{M}(\alpha, \chi) \to \hat{P}\hat{M}(\alpha, \chi)$. First we consider the impact of the free evolution on $\hat{U}_1^2$.

$$\hat{U}_1^2 = \left[\hat{P}_\pi\hat{M}(-\frac{\pi}{2}, 0)\hat{K}_1^{\frac{1}{2}}\hat{P}_\pi\hat{M}(\frac{\pi}{2}, 0)\hat{P}_\pi\hat{M}(-\frac{\pi}{2}, \frac{\pi}{2})\hat{K}_2\hat{P}_\pi\hat{M}(\frac{\pi}{2}, \frac{\pi}{2})\hat{P}_\pi\hat{M}(-\frac{\pi}{2}, 0)\hat{K}_1^{\frac{1}{2}}\hat{P}_\pi\hat{M}(\frac{\pi}{2}, 0) \right]^2 \tag{51}$$

$$= \hat{P}_\pi\hat{M}(-\frac{\pi}{2}, 0)\hat{K}_1^{\frac{1}{2}}\hat{M}(\frac{\pi}{2}, 0)\hat{M}(-\frac{\pi}{2}, \frac{\pi}{2})\hat{T}(\pi)\hat{K}_2\hat{M}(\frac{\pi}{2}, \frac{\pi}{2})\hat{M}(-\frac{\pi}{2}, 0)\hat{T}(\pi)\hat{K}_1^{\frac{1}{2}}\hat{M}(\frac{\pi}{2}, 0)$$
$$\cdot \hat{M}(-\frac{\pi}{2}, 0)\hat{T}(\pi)\hat{K}_1^{\frac{1}{2}}\hat{M}(\frac{\pi}{2}, 0)\hat{M}(-\frac{\pi}{2}, \frac{\pi}{2})\hat{T}(\pi)\hat{K}_2\hat{M}(\frac{\pi}{2}, \frac{\pi}{2})\hat{M}(-\frac{\pi}{2}, 0)\hat{T}(\pi)\hat{K}_1^{\frac{1}{2}}\hat{P}_\pi\hat{M}(\frac{\pi}{2}, 0) \tag{52}$$

$$= \hat{P}_\pi\hat{M}(-\frac{\pi}{2}, 0)\hat{K}_1^{\frac{1}{2}}\hat{M}(\frac{\pi}{2}, 0)\hat{M}(-\frac{\pi}{2}, \frac{\pi}{2})\hat{K}_2^{-1}\hat{M}(\frac{\pi}{2}, \frac{\pi}{2})\hat{M}(-\frac{\pi}{2}, 0)\hat{T}(2\pi)\hat{K}_1^{\frac{1}{2}}\hat{M}(\frac{\pi}{2}, 0)$$
$$\cdot \hat{M}(-\frac{\pi}{2}, 0)\hat{K}_1^{-\frac{1}{2}}\hat{M}(\frac{\pi}{2}, 0)\hat{M}(-\frac{\pi}{2}, \frac{\pi}{2})\hat{T}(2\pi)\hat{K}_2\hat{M}(\frac{\pi}{2}, \frac{\pi}{2})\hat{M}(-\frac{\pi}{2}, 0)\hat{K}_1^{-\frac{1}{2}}\hat{P}_\pi\hat{M}(\frac{\pi}{2}, 0) \tag{53}$$

$$= \hat{P}_\pi\hat{M}(-\frac{\pi}{2}, 0)\hat{K}_1^{\frac{1}{2}}\hat{M}(\frac{\pi}{2}, 0)\hat{M}(-\frac{\pi}{2}, \frac{\pi}{2})\hat{K}_2^{-1}\hat{M}(\frac{\pi}{2}, \frac{\pi}{2})\hat{M}(-\frac{\pi}{2}, 0)\hat{K}_1^{\frac{1}{2}}\hat{M}(\frac{\pi}{2}, 0)$$
$$\cdot \hat{M}(-\frac{\pi}{2}, 0)\hat{K}_1^{-\frac{1}{2}}\hat{M}(\frac{\pi}{2}, 0)\hat{M}(-\frac{\pi}{2}, \frac{\pi}{2})\hat{K}_2\hat{M}(\frac{\pi}{2}, \frac{\pi}{2})\hat{M}(-\frac{\pi}{2}, 0)\hat{K}_1^{-\frac{1}{2}}\hat{P}_\pi\hat{M}(\frac{\pi}{2}, 0) \tag{54}$$

$$= \hat{P}_\pi^2 \tag{55}$$

$$= \hat{T}(\pi) \tag{56}$$

In the last step, we have used that from the first to the second line in the equation above we find inverse MW-rotations next to each other. Subsequently, inverse operators line up next to each other so all that remains are the $\hat{P}_\pi$-operators in the front and the end of the equation. For arbitrary t one can give the following case distinction:

$$\hat{U}_1^t = \begin{cases} \mathbf{1} & t \bmod 4 = 0 \\ \hat{P}_\pi\hat{M}(-\frac{\pi}{2}, 0)\hat{K}_1^{\frac{1}{2}}\hat{M}(\frac{\pi}{2}, 0)\hat{M}(-\frac{\pi}{2}, \frac{\pi}{2})\hat{K}_2^{-1}\hat{M}(\frac{\pi}{2}, \frac{\pi}{2})\hat{M}(-\frac{\pi}{2}, 0)\hat{K}_1^{\frac{1}{2}}\hat{P}_\pi\hat{M}(\frac{\pi}{2}, 0) & t \bmod 4 = 1 \\ \hat{T}(\pi) & t \bmod 4 = 2 \\ \hat{P}_\pi\hat{M}(-\frac{\pi}{2}, 0)\hat{K}_1^{-\frac{1}{2}}\hat{M}(\frac{\pi}{2}, 0)\hat{M}(-\frac{\pi}{2}, \frac{\pi}{2})\hat{K}_2\hat{M}(\frac{\pi}{2}, \frac{\pi}{2})\hat{M}(-\frac{\pi}{2}, 0)\hat{K}_1^{-\frac{1}{2}}\hat{P}_\pi\hat{M}(\frac{\pi}{2}, 0) & t \bmod 4 = 3 \end{cases} \tag{57}$$

Since the calculation of $\hat{U}_2^2$ follows in a completely analogous fashion, one can just write down the result.

$$\hat{U}_2^t = \begin{cases} \mathbf{1} & t \bmod 4 = 0 \\ \hat{P}_\pi\hat{M}(-\frac{\pi}{2}, \frac{\pi}{2})\hat{K}_2^{\frac{1}{2}}\hat{M}(\frac{\pi}{2}, \frac{\pi}{2})\hat{M}(-\frac{\pi}{2}, 0)\hat{K}_1^{-1}\hat{M}(\frac{\pi}{2}, 0)\hat{M}(-\frac{\pi}{2}, \frac{\pi}{2})\hat{K}_2^{\frac{1}{2}}\hat{P}_\pi\hat{M}(\frac{\pi}{2}, \frac{\pi}{2}) & t \bmod 4 = 1 \\ \hat{T}(\pi) & t \bmod 4 = 2 \\ \hat{P}_\pi\hat{M}(-\frac{\pi}{2}, \frac{\pi}{2})\hat{K}_2^{-\frac{1}{2}}\hat{M}(\frac{\pi}{2}, \frac{\pi}{2})\hat{M}(-\frac{\pi}{2}, 0)\hat{K}_1\hat{M}(\frac{\pi}{2}, 0)\hat{M}(-\frac{\pi}{2}, \frac{\pi}{2})\hat{K}_2^{-\frac{1}{2}}\hat{P}_\pi\hat{M}(\frac{\pi}{2}, \frac{\pi}{2}) & t \bmod 4 = 3 \end{cases} \tag{58}$$

In summary, the finite MW-ontime of $\tau = \pi$ causes every second kick operator to be inverted. Considering the evolution as a Floquet-problem, this causes inverse operators to end up next to each other. This again results in the configuration being antiresonant. Therefore it is impossible in the „Floquet-protocol" to measure the MCD for higher timesteps then $t = 1$. Since from Eq. (34) the MCD converges upon the winding number only for an average over many $C_l(T)$, executing the experiment within this protocol using a MW ontime of $\tau = \pi$ is not possible.

4.2 Resonant protocol

Rewriting of the operators as in Eq. (44), (45) can be understood in the following manner: Since the kicks can not be executed in σ_x or σ_y direction the system has to be rotated, so an equivalent kick is created by actually applying a σ_z pulse. Afterward, the system is rotated back to its original „orientation".

Both $\hat{U}_1$ and $\hat{U}_2$ have kicks of half strength at their beginning and ending, to assure chiral symmetry. When the operators are applied subsequently, pay attention to the section in the protocol where two kicks of half strength follow directly upon each other. First, we have a forward rotation to apply the kick, followed by a rotation back to the original orientation. This section repeats. Consequently in between one rotates backward and forward again to apply the second kick of half strength. In other words, the MW rotations in between serve no purpose, since they are inverse to each other. Look for example at the corresponding sequence of $\hat{U}_1$.

$$\hat{M}(-\frac{\pi}{2},0)\hat{K}_1^{\frac{1}{2}}\hat{M}(\frac{\pi}{2},0)\hat{M}(-\frac{\pi}{2},0)\hat{K}_1^{\frac{1}{2}}\hat{M}(\frac{\pi}{2},0) = \hat{M}(-\frac{\pi}{2},0)\hat{K}_1^{\frac{1}{2}}\hat{K}_1^{\frac{1}{2}}\hat{M}(\frac{\pi}{2},0) = \hat{M}(-\frac{\pi}{2},0)\hat{K}_1\hat{M}(\frac{\pi}{2},0) \quad (59)$$

Exploiting this, the number of necessary MW applications can be reduced and the protocol can be rewritten.

$$\hat{U}_1^t = \hat{M}(-\frac{\pi}{2},0)\hat{K}_1^{\frac{1}{2}}\hat{M}(\frac{\pi}{2},0)\left[\hat{M}(-\frac{\pi}{2},\frac{\pi}{2})\hat{K}_2\hat{M}(\frac{\pi}{2},\frac{\pi}{2})\hat{M}(-\frac{\pi}{2},0)\hat{K}_1\hat{M}(\frac{\pi}{2},0)\right]^{t-1}$$
$$\cdot \hat{M}(-\frac{\pi}{2},\frac{\pi}{2})\hat{K}_2\hat{M}(\frac{\pi}{2},\frac{\pi}{2})\hat{M}(-\frac{\pi}{2},0)\hat{K}_1^{\frac{1}{2}}\hat{M}(\frac{\pi}{2},0) \quad (60)$$

$$\hat{U}_2^t = \hat{M}(-\frac{\pi}{2},\frac{\pi}{2})\hat{K}_2^{\frac{1}{2}}\hat{M}(\frac{\pi}{2},\frac{\pi}{2})\left[\hat{M}(-\frac{\pi}{2},0)\hat{K}_1\hat{M}(\frac{\pi}{2},0)\hat{M}(-\frac{\pi}{2},\frac{\pi}{2})\hat{K}_2\hat{M}(\frac{\pi}{2},\frac{\pi}{2})\right]^{t-1}$$
$$\cdot \hat{M}(-\frac{\pi}{2},0)\hat{K}_1\hat{M}(\frac{\pi}{2},0)\hat{M}(-\frac{\pi}{2},\frac{\pi}{2})\hat{K}_2^{\frac{1}{2}}\hat{M}(\frac{\pi}{2},\frac{\pi}{2}) \quad (61)$$

Again the finite MW-ontime is introduced by substituting $\hat{M}(\alpha,\chi) \to \hat{P}_\pi\hat{M}(\alpha,\chi)$. Since again the calculations for $\hat{U}_1^t$ and $\hat{U}_2^t$ are analogous we will just present it for the first evolution operator.

$$\hat{U}_1^t = \hat{P}_\pi\hat{M}(-\frac{\pi}{2},0)\hat{K}_1^{\frac{1}{2}}\hat{P}_\pi\hat{M}(\frac{\pi}{2},0)\left[\hat{P}_\pi\hat{M}(-\frac{\pi}{2},\frac{\pi}{2})\hat{K}_2\hat{P}_\pi\hat{M}(\frac{\pi}{2},\frac{\pi}{2})\hat{P}_\pi\hat{M}(-\frac{\pi}{2},0)\hat{K}_1\hat{P}_\pi\hat{M}(\frac{\pi}{2},0)\right]^{t-1}$$
$$\cdot \hat{P}_\pi\hat{M}(-\frac{\pi}{2},\frac{\pi}{2})\hat{K}_2\hat{P}_\pi\hat{M}(\frac{\pi}{2},\frac{\pi}{2})\hat{P}_\pi\hat{M}(-\frac{\pi}{2},0)\hat{K}_1^{\frac{1}{2}}\hat{P}_\pi\hat{M}(\frac{\pi}{2},0) \quad (62)$$

$$= \hat{P}_\pi\hat{M}(-\frac{\pi}{2},0)\hat{K}_1^{\frac{1}{2}}\hat{M}(\frac{\pi}{2},0)\left[\hat{M}(-\frac{\pi}{2},\frac{\pi}{2})\hat{T}(\pi)\hat{K}_2\hat{M}(\frac{\pi}{2},\frac{\pi}{2})\hat{M}(-\frac{\pi}{2},0)\hat{T}(\pi)\hat{K}_1\hat{M}(\frac{\pi}{2},0)\right]^{t-1}$$
$$\cdot \hat{M}(-\frac{\pi}{2},\frac{\pi}{2})\hat{T}(\pi)\hat{K}_2\hat{M}(\frac{\pi}{2},\frac{\pi}{2})\hat{M}(-\frac{\pi}{2},0)\hat{T}(\pi)\hat{K}_1^{\frac{1}{2}}\hat{P}_\pi\hat{M}(\frac{\pi}{2},0) \quad (63)$$

$$= \hat{P}_\pi\hat{M}(-\frac{\pi}{2},0)\hat{K}_1^{\frac{1}{2}}\hat{M}(\frac{\pi}{2},0)\left[\hat{M}(-\frac{\pi}{2},\frac{\pi}{2})\hat{K}_2^{-1}\hat{M}(\frac{\pi}{2},\frac{\pi}{2})\hat{M}(-\frac{\pi}{2},0)\hat{T}(2\pi)\hat{K}_1\hat{M}(\frac{\pi}{2},0)\right]^{t-1}$$
$$\cdot \hat{M}(-\frac{\pi}{2},\frac{\pi}{2})\hat{K}_2^{-1}\hat{M}(\frac{\pi}{2},\frac{\pi}{2})\hat{M}(-\frac{\pi}{2},0)\hat{T}(2\pi)\hat{K}_1^{\frac{1}{2}}\hat{P}_\pi\hat{M}(\frac{\pi}{2},0) \quad (64)$$

$$= \hat{P}_\pi\hat{M}(-\frac{\pi}{2},0)\hat{K}_1^{\frac{1}{2}}\hat{M}(\frac{\pi}{2},0)\left[\hat{M}(-\frac{\pi}{2},\frac{\pi}{2})\hat{K}_2^{-1}\hat{M}(\frac{\pi}{2},\frac{\pi}{2})\hat{M}(-\frac{\pi}{2},0)\hat{K}_1\hat{M}(\frac{\pi}{2},0)\right]^{t-1}$$
$$\cdot \hat{M}(-\frac{\pi}{2},\frac{\pi}{2})\hat{K}_2^{-1}\hat{M}(\frac{\pi}{2},\frac{\pi}{2})\hat{M}(-\frac{\pi}{2},0)\hat{K}_1^{\frac{1}{2}}\hat{P}_\pi\hat{M}(\frac{\pi}{2},0) \quad (65)$$

In other words: Every second kick-operator in the sequence gets inverted. In this protocol the second kick operator is now exclusively $\hat{K}_2$, so no operator annihilation happens. As stated above, analogous calculations can be made for $\hat{U}_2$.

$$\hat{U}_2^t = \hat{P}_\pi\hat{M}(-\frac{\pi}{2},\frac{\pi}{2})\hat{K}_2^{\frac{1}{2}}\hat{M}(\frac{\pi}{2},\frac{\pi}{2})\left[\hat{M}(-\frac{\pi}{2},0)\hat{K}_1^{-1}\hat{M}(\frac{\pi}{2},0)\hat{M}(-\frac{\pi}{2},\frac{\pi}{2})\hat{K}_2\hat{M}(\frac{\pi}{2},\frac{\pi}{2})\right]^{t-1}$$
$$\cdot \hat{M}(-\frac{\pi}{2},0)\hat{K}_1^{-1}\hat{M}(\frac{\pi}{2},0)\hat{M}(-\frac{\pi}{2},\frac{\pi}{2})\hat{K}_2^{\frac{1}{2}}\hat{P}_\pi\hat{M}(-\frac{\pi}{2},\frac{\pi}{2}) \quad (66)$$

At this point, it is probably useful for better understanding to grasp the difference between the resonant and the antiresonant protocol in a more simplified scheme. Due to the similarity between the two chiral symmetric

operators, we simply focus on U_1. For the sake of clarity, the MW rotations and translation operators are not written down in the scheme presented below. The operators inverted by the impact of the free evolution are printed in red.

<div align="center">

Antiresonant case

$$\hat{U}_1^2 = \hat{K}_1^{\frac{1}{2}}\hat{K}_2\hat{K}_1^{\frac{1}{2}}\hat{K}_1^{\frac{1}{2}}\hat{K}_2\hat{K}_1^{\frac{1}{2}}$$

$$\underset{\text{Free evolution}}{\rightarrow} \quad \hat{K}_1^{\frac{1}{2}}\textcolor{red}{\hat{K}_2^{-1}}\hat{K}_1^{\frac{1}{2}}\textcolor{red}{\hat{K}_1^{-\frac{1}{2}}}\hat{K}_2\textcolor{red}{\hat{K}_1^{-\frac{1}{2}}}$$

$$= \hat{K}_1^{\frac{1}{2}}\textcolor{red}{\hat{K}_2^{-1}}\hat{K}_2\textcolor{red}{\hat{K}_1^{-\frac{1}{2}}}$$

$$= \hat{K}_1^{\frac{1}{2}}\textcolor{red}{\hat{K}_1^{-\frac{1}{2}}}$$

$$= \mathbf{1}$$

Resonant case

$$\hat{U}_1^2 = \hat{K}_1^{\frac{1}{2}}\hat{K}_2\hat{K}_1\hat{K}_2\hat{K}_1^{\frac{1}{2}}$$

$$\underset{\text{Free evolution}}{\rightarrow} \quad \hat{K}_1^{\frac{1}{2}}\textcolor{red}{\hat{K}_2^{-1}}\hat{K}_1\textcolor{red}{\hat{K}_2^{-1}}\hat{K}_1^{\frac{1}{2}}$$

</div>

4.3 Symmetry inversion in local space

For the resonant case, there is no operator annihilation, but still, every second operator experiences an inversion. This is equivalent to the statement that within the kick operators $\hat{K}_1$ and $\hat{K}_2$, the sinus and cosinus are interchanged. This can be understood if instead of its square one identifies the operator $\hat{P}_\pi$ with a shift in local space. Since it is not entirely trivial that this equivalence holds, it is explained in full detail in B.3. Now consider that every kick is framed by two MW rotations:

$$\hat{M}(\alpha_1,\chi_1)\hat{K}(\theta)_j\hat{M}(\alpha_2,\chi_2) \rightarrow e^{-i\frac{\hat{n}}{2}\pi}\hat{M}(\alpha_1,\chi_1)\hat{K}(\theta)_j \; e^{-i\frac{\hat{n}}{2}\pi}\hat{M}(\alpha_2,\chi_2) \tag{67}$$

$$= \hat{M}(\alpha_1,\chi_1)e^{-i\frac{\hat{n}}{2}\pi}\hat{K}(\theta)_j \; e^{i\frac{\hat{n}}{2}\pi}e^{-i\hat{n}\pi}\hat{M}(\alpha_2,\chi_2) \tag{68}$$

$$= \hat{M}(\alpha_1,\chi_1)\hat{K}(\theta+\frac{\pi}{2})_j \; e^{-i\hat{n}\pi}\hat{M}(\alpha_2,\chi_2) \tag{69}$$

The remaining shift operator $e^{-i\hat{n}\pi} \equiv \hat{T}(\pi)$ causes the already known inversion of every second kick, causing the protocol to be either resonant or antiresonant respectively. Taking a look at how precisely the kick operators $\hat{K}_1$ and $\hat{K}_2$ from Eq. (46), (47) are affected by the shift from including the free evolution, one finds for their dependency in angular momentum:

$$\sin(\theta+\frac{\pi}{2}) \rightarrow \cos(\theta) \tag{70}$$

$$\cos(\theta+\frac{\pi}{2}) \rightarrow \textcolor{red}{-}-\sin(\theta) = \sin(\theta) \tag{71}$$

The second minus for the sinus comes from the $\theta = \pi$ shift of every second operator within the resonant protocol. In fact, the consideration of finite ontime of $\tau = \pi$ for the MW causes the MCD and thus by Eq. (34) the topological measurements to experience a change in sign. It is rather clear that here the reason is to be found in a symmetry change in local space. As shown in Fig. 8, the cause for that are the momentum distributions of the internal states to be mirrored at zero momentum class. It turns out that only the relative shift of the kicks from $\hat{K}_1$ to $\hat{K}_2$ being $\pm\frac{\pi}{2}$ determines the direction of evolution of the internal states. Thus, one can assign to the kick sequence in local space an „orientation" number ± 1, that determines the direction of evolution.
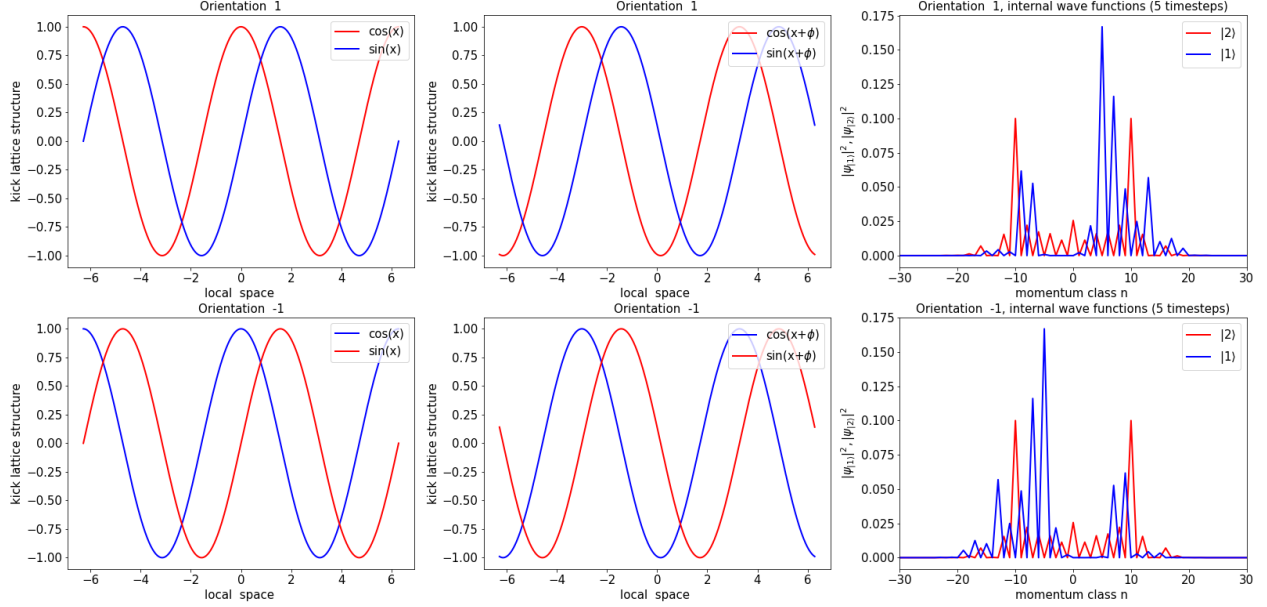
Figure 8: Orientation change in local space. The upper images illustrate „orientation 1“, the lower ones „orientation -1“. The first two images in each row intend to illustrate two equivalent configurations of the kick lattice structure. One could assume for example that the „red kick“ appears first in the protocol, followed by the „blue kick“. Then the relative shift of the kicks is changed from one orientation to the other. The rightmost images show the momentum distributions of the internal states for the corresponding orientation. It is shown that the change of orientation mirrors the distributions at zero momentum. Here, by the choice of the initial state $|\psi_{in}\rangle = |2\rangle \otimes |n = 0\rangle$ the state $|2\rangle$ evolves symmetrically in momentum space. That effect will be discussed in more detail in Sec. 4.5.

In summary, if finite MW ontime of $\tau = \pi$ is considered in the resonant protocol, the orientation of the kick lattice changes. This way the momentum distribution for both of the internal states is caused to evolve in opposite direction. Thus the momentum expectation value for each internal state changes the sign, and since the MCD from Eq. (33) is computed by the difference of the momentum expectation values of the internal states, it also changes sign. When then the topological number is computed by Eq. (34), it becomes clear that also here a change in the sign will be found.

It is important to note that the change of sign is effectively only a result from the inversion of the lattice structure in local space and the underlying physical theory from Sec. 2.5 on topological phase transitions is left unaffected.

4.4 Compensation of sign

Since the change of sign within the topological number is due to the change of orientation discussed above, it can be compensated by changing the orientation back to the original configuration. One option to do this would be to change the phases within the MW rotations. Therefore focus on the following sequence of the evolution operators:

$$\hat{M}(-\frac{\pi}{2},0)e^{-ik_1\cos(\theta)\sigma_z}\hat{M}(\frac{\pi}{2},0) = \hat{M}(\frac{\pi}{2},0)e^{ik_1\cos(\theta)\sigma_z}\hat{M}(-\frac{\pi}{2},0) \tag{72}$$

A proof for Eq. (72) is given in Ref. B.4. The change suggested here would compensate for the additional minus sign in the exponent coming from the free evolution.

4.5 Symmetry in the evolution

If one of the internal states evolves symmetrically in momentum space it becomes irrelevant for the measurement of the MCD. In this case, its momentum expectation-value is zero and this state does not contribute to the MCD. Therefore all the information about the topological winding number would be contained in the other internal state. Since the MCD measures the difference in the expectation-value in the momentum distribution of the two internal states, the momentum-expectation value for the internal would need to be measured respectively. If it would be sufficient to measure only one instead of two internal states, the amount of experimental effort could be significantly reduced. In the following, some observations from numerical experiments will be presented.

1) If one of the internal states, for example, $|2\rangle$ is defined to be a symmetric initial state in momentum-space and the state $|1\rangle$ has no contribution to the wavefunction (e.g. $|\psi_{in}\rangle = |2\rangle \otimes |n = 0\rangle$), then the $|2\rangle$-state will continue to evolve symmetrically around the symmetry-axis of the initial state. Therefore the information for the winding number is completely carried by the $|1\rangle$-state.
2) If the initial state still has no contribution by $|1\rangle$, but the initial state is not defined symmetrically in $|2\rangle$, then the state $|2\rangle$ does not evolve symmetrically and again both internal states contribute to the MCD.
3) If the initial state has a contribution of $|1\rangle$ and $|2\rangle$, then both internal states contribute to the MCD and none can be neglected.

If, of course, we are in case 1) and thus the momentum expectation value of one of the internal states is zero, it is not necessary to measure for a specific internal state at all. Here one could simply measure $P(t) = P(t)_{|1\rangle} + P(t)_{|2\rangle}$. From this distribution it is possible to calculate the expectation value, which then becomes identical to the MCD: $\langle P_{1,2}(t)\rangle \equiv C_{1,2}(t)$. This would enable us to use the same measurement apparatus as the one already used for the quantum walk experiment in Ref. [4].

4.6 Stability

As already mentioned above, the impact of lattice vibrations has already been numerically investigated in Ref. [6]. Furthermore, the precise timing of the internal rotation of the atom is practically unknown within the experimental realization. This uncertainty leads effectively to fluctuations within the second argument in the MW rotation $\hat{M}(\alpha, \chi)$ among the ensemble of atoms. This section will focus furthermore on the stability of the system under the impact of such phase fluctuations.

4.6.1 Numerical framework regarding stability, simulations

The simulations will measure the MCD from Eq. (33) for fixed $k_1 = \pi/2$, while $k_2 \in [0, 2.5\pi]$ is scanned. k_1 and k_2 are chosen to create comparable images to Ref. [5,6]. Using Eq. (34), for each configuration for k_1, k_2 the topological winding number will be computed for five applications of the evolution operator $\hat{U}_{1,2}$. Five of such timesteps are considered to lie in an experimentally accessible range. The following function, furthermore referred to as „fidelity", is defined to quantify the impact of the perturbation on the system.

$$F_i(\Delta) = \int_{0.4}^{2.5\pi} \Big| \frac{\bar{C}_{i_{\text{unperturbed}}}(k_2) - \bar{C}_{i_{\text{perturbed}}}(\Delta, k_2)}{(2.5\pi - 0.4) * \bar{C}_{i_{\text{unperturbed}}}(k_2)} \Big| dk_2 \tag{73}$$

The fidelity is dependent on the strength of the perturbation Δ. Fundamentally it computes the difference between the perturbed and the unperturbed topological curve over the full range of k_2. Additionally, the function is rescaled by the integral of the unperturbed curve and the range of integration. This way it is ensured that it returns zero if the system is unperturbed and one if the signal has fully decayed. The lower border of integration is chosen above zero because the curves show a transition to the first plateau already seen in Fig. 3, that does not appear in the phase diagram presented in Ref. [5]. Thus this range is excluded for the fidelity. Every data point in the simulations is calculated for 1000 realizations, resolving in a good convergence.
The phase fluctuations are implemented as the following:

$$\hat{M}(\alpha, \chi) \rightarrow \hat{M}(\alpha, \chi + \Delta_\chi) \tag{74}$$

Since it is not entirely obvious how the MW phase fluctuations would look like in detail, several models are studied. These models differ in the way in which the random number Δ_χ is chosen within the simulation. The models under investigation are the following:

Model 1: „static" phase = one random number per realization, fixed for all MW´s
$$\Delta_\chi \in \text{uniform}[-\Delta, \Delta]$$
Model 2: „dynamic 1" phase = one random number per MW application
$$\Delta_\chi \in \text{uniform}[-\Delta, \Delta]$$
Model 3: „dynamic 2" phase = phase accumulation within one realization
$$\Delta_{\chi n} = \sum_{i=1}^{n} = \delta_{\chi i}, \text{ with } \delta_{\chi i} \in \text{uniform}[-\Delta, \Delta]$$
$\delta_{\chi i}$ is drawn individually for each MW application

The last model corresponds to a „phase-drift " and describes an open quantum system. Since it assumes a dependency from one fluctuation in the MW rotation to the next, it is probably the most realistic of the three models.

In the last step one also has to consider the free evolution without neglecting quasimomentum, to simulate the condition of the system at finite temperature. Since we focus on the case $\tau = \pi$ we are only interested in the resonant case from Sec. 4.2 and below. In the considerations so far quasimomentum has always been neglected. Now a quasimomentum distribution of finite width is included by Eq. (43). The random numbers for the β-distribution are drawn again from a Gaussian distribution, here centered at $\mu = 0$ and $\sigma = 0.01\hbar G$.

4.6.2 Simulations

Fig. 9, 10, 11 below show the implementation of what is discussed in Sec. 4.6.1. Left, the fidelity curve in dependency of the range Δ, from which the random numbers simulating the fluctuations are drawn, is shown. The image in the center shows an example of the deformation of the topological step function at $\Delta = \pi/6$, while in the rightmost image the impact of adding finite quasimomentum is illustrated. The change of sign from the resonant protocol is compensated, as suggested in Sec. 4.4.

Similar images to Fig. 9, 10, 11 can be found in B.5, exploiting the symmetry from Sec. 4.5 by measuring the momentum distribution of only one internal state. These images again show fundamentally a similar behaviour to what is seen in Fig. 9, 10, 11.

We conclude that the static-phase model has only a very weak dependency on the introduction of phase noise. Even for large fluctuations, no significant deviation can be observed from the fidelity curve. Both the dynamic phase models display a stronger dependency on the range of fluctuations. The fidelity curves converge to one (full signal loss) rather quickly, after passing a critical threshold at approximately $\Delta = \frac{\pi}{2}$. These models suggest that the fluctuations in phase need to be kept under control if the topological phase transitions shall stay observable. Even though more deformed in the „phase-drift" model from Fig. 11, the exemplary images at $\Delta = \frac{\pi}{6}$ suggests that if the phase noise is kept under a sufficient amount of control, the topological steps are still well observable. For a better interpretation of the fidelity curves, consult Fig. 19,
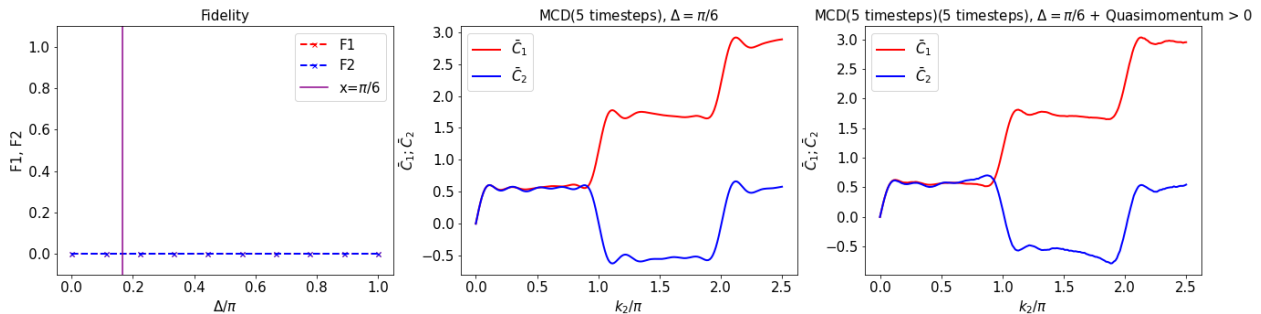

Figure 9: Implementation of Model 1. The fidelity shows a weak dependency on the range of phase fluctuations Δ. Thus the exemplary image at $\Delta = \frac{\pi}{6}$ is close to the ideal case for 5 steps in the evolution. It is seen that quasimomentum is distorting the steps slightly. The simulation is implemented for 1000 realizations and both internal states are measured to compute the MCD. The initial state is given by $|\psi_{in}\rangle = |2\rangle \otimes |n = 0\rangle$.

Figure 10: Implementation of Model 2. The fidelity shows a strong dependency on the range of phase fluctuations Δ. The exemplary image at $\Delta = \frac{\pi}{6}$ shows already some perturbations within the topological curve. The impact of quasimomentum leads to some additional deformation but does not pose a great threat to the „survival" of the steps, as long the phase noise within the MW is controlled. The simulation is implemented for 1000 realizations and both internal states are measured to compute the MCD. The initial state is given by $|\psi_{in}\rangle = |2\rangle \otimes |n = 0\rangle$.
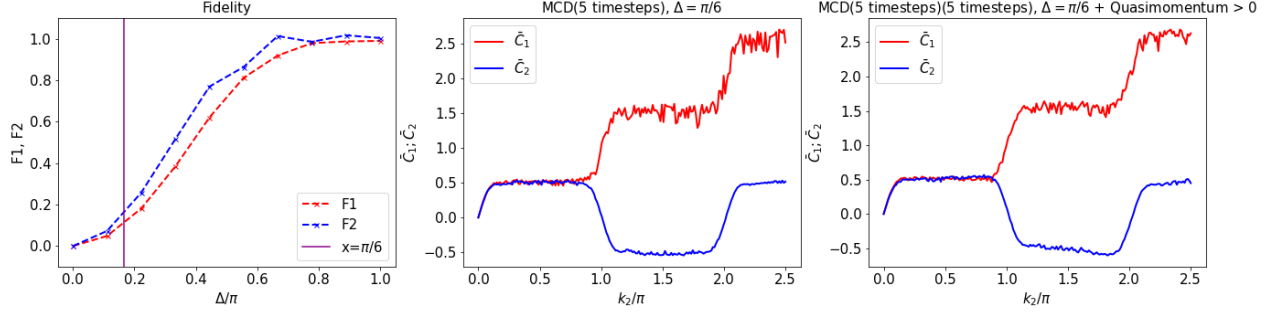

Figure 11: Implementation of Model 3. The fidelity shows a strong dependency on the range length of the steps within the phase drift, dependent on Δ. The exemplary image at $\Delta = \frac{\pi}{6}$ shows already stronger deformations within the topological curve, even though the steps stay visible. The impact of quasimomentum does not significantly contribute to the deformation of the curve. The simulation is implemented for 1000 realizations and both internal states are measured to compute the MCD. The initial state is given by $|\psi_{in}\rangle = |2\rangle \otimes |n = 0\rangle$.
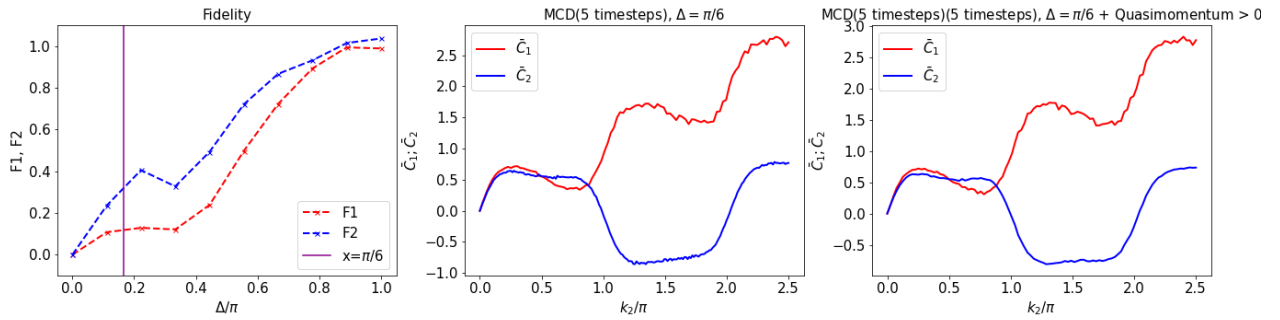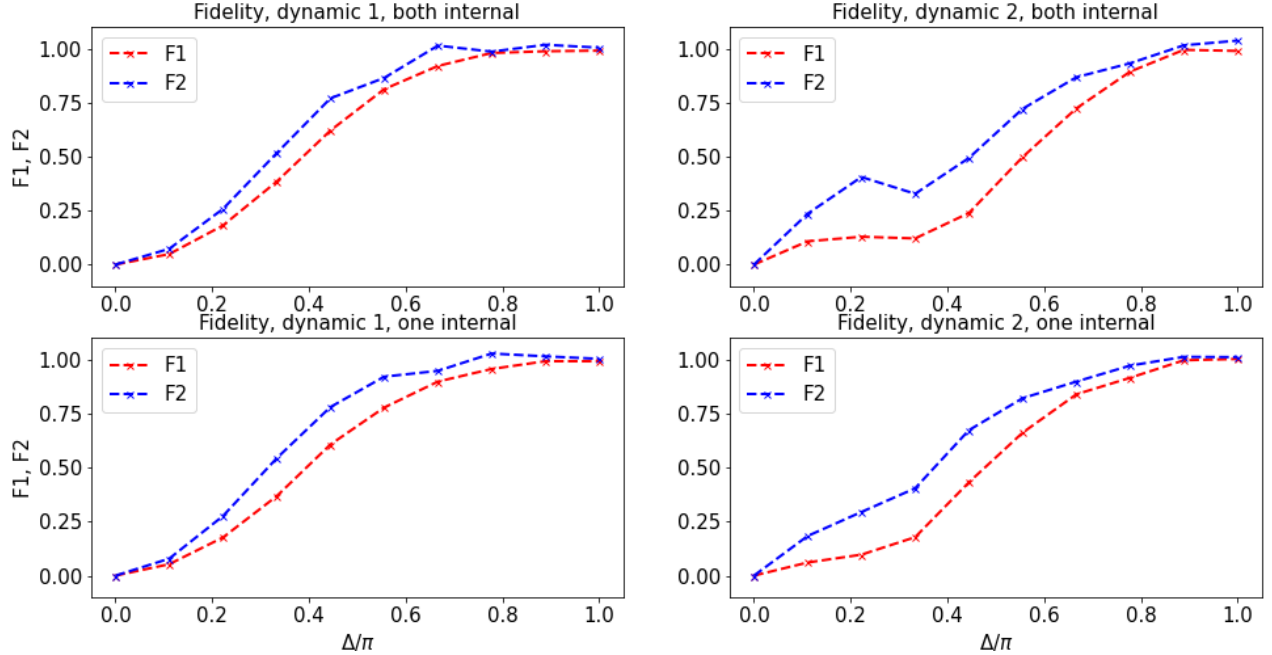
Figure 12: Demonstrated are the fidelity curves for both dynamic phase models. In the upper images, the curve is created by measuring the MCD including both internal states. The lower images exploit the symmetry from Sec. 4.5. It can be concluded that even though the symmetry is broken by perturbations to the system, the stability towards these perturbations is comparable for both cases. Since no significant negative influence can be seen by simplifying the measurement process, the suggestion from Sec. 4.5 remains reasonable. Every data point is taken from implementation with 1000 realizations. The initial state is given by $|\psi_{in}\rangle = |2\rangle \otimes |n = 0\rangle$.

explicitly showing the phase decay in dependency of Δ.

Within all three models, the impact of quasimomentum plays a subordinate role. Consider the benefits of the resonant protocol, which allows for a MW ontime of $\tau = \pi$ while reducing the amount of MW rotations and thus the number of free evolution operators. As stated above, the ideal evolution operator becomes unity for $\tau = 4\pi$, the full Talbot time. The resonant protocol from Sec. 4.2 allows to drastically reduce the duration of the free evolution down to $\tau = \pi$ as a new resonance condition. If quasimomentum is considered, the resonance condition is slightly violated. This deviation from perfectly resonant case gets enlarged, the longer the duration of the MW rotation. Consult Eq. (9). Thus, the resonant protocol allows reducing the impact of violation of the resonance condition on the protocol by holding the MW duration rather short.

If it is of interest to exploit the symmetry discussed in Sec. 4.5, one has to consider that this symmetry is broken if perturbations from the ideal case are considered. This raises the question of whether this break of symmetry would be too large to be exploited. The consequence would be that both internal state momentum distributions would need to be measured anyways. However, the fidelity curves from Fig. 12 do not suggest such thing. They state that the deviation from the unperturbed case increase in a similar way whether both states are measured or only one, accordingly to Sec. 4.5.

4.7 Light shift

So far the influence of the $\cos^2$-terms from Sec. 1.2.4 have been implicitly assumed to be fully compensated. Numerical tests showed that the topological signal fully decays if the light-shift effects are included. Thus the light shift effects must be at least partially be compensated. Since we have two operators $\hat{K}_1$ and $\hat{K}_2$ with different kick strengths, it might be hard to compensate for both at once. The suggestion is to only compensate for the operator at constant kick strength $\hat{K}_1$. The compensation is proposed in the following
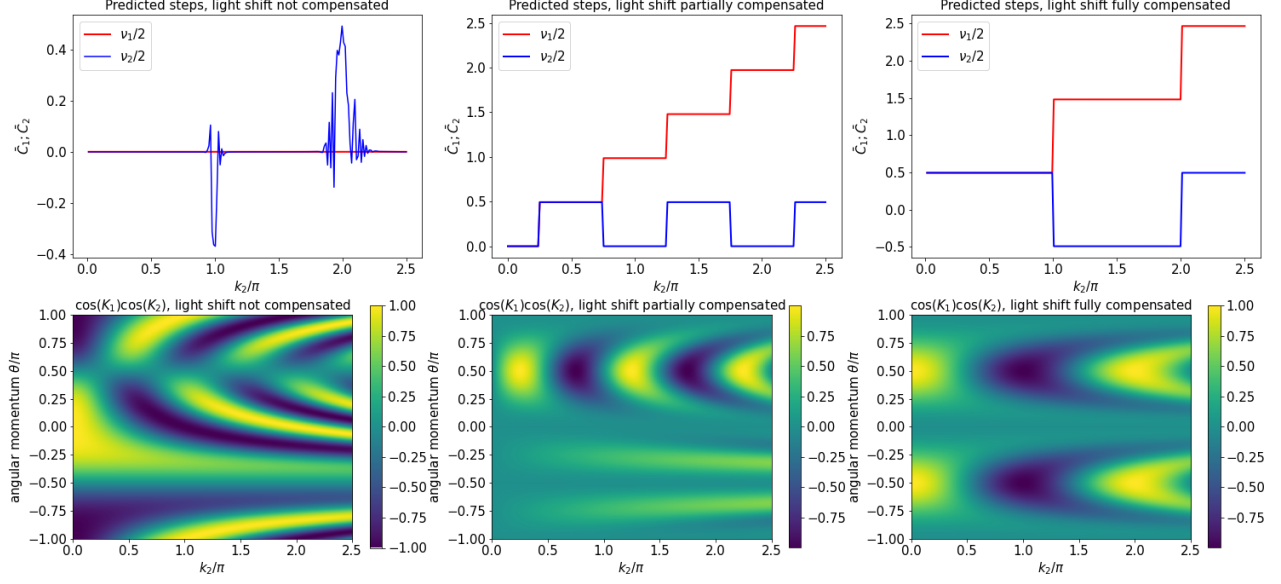
Figure 13: The upper plots show the theoretical prediction for the steps in different stages of compensation of the light shift. The lower images show the value of the function $\cos(K_1)\cos(K_2)$ within the configuration space. The bandgap and thus the topological winding number can only change if this function is equal to ± 1. Note that this condition is fulfilled at the phase transitions for the partially and fully compensated case. Within the uncompensated case, it appears that this function is almost ± 1 across the full range of k_2, implying instability for the topological phases.

way:

$$\hat{K}_1 = \begin{pmatrix} e^{-ik_1\cos(\theta)} & 0 \\ 0 & e^{ik_1\cos(\theta)} \end{pmatrix} \rightarrow \qquad\qquad \begin{pmatrix} e^{-ik_1\cos(\theta)} & 0 \\ 0 & e^{ik_1\cos(\theta)} \end{pmatrix} \qquad (75)$$

$$\hat{K}_2 = \begin{pmatrix} e^{-ik_2\sin(\theta)} & 0 \\ 0 & e^{ik_2\sin(\theta)} \end{pmatrix} \rightarrow \begin{pmatrix} e^{-i(k_2-k_1)} & 0 \\ 0 & e^{ik(k_2-k_1)} \end{pmatrix} \begin{pmatrix} e^{-ik_2\sin(\theta)} & 0 \\ 0 & e^{ik_2\sin(\theta)} \end{pmatrix} \qquad (76)$$

With the equations from Sec. 2.5 one is able to conduct predictions for the topological steps of the altered operators $\hat{U}_1$ and $\hat{U}_2$. One simply implements $K_1 = k_1\cos(\theta)$ and $K_2 = k_2(\sin(\theta)+1) - k_1$ for Eq. (31), (32). Analogous calculation can be done for the fully uncompensated case. The results are presented in Fig. 13.

Note that the fully uncompensated case indicates topological instability, seen by the plot of $\cos(K_1)\cos(K_2)$ within the configuration space. Even though the operators trivially conserve chiral symmetry if the light shift is introduced, it appears that within this configuration the bandgap might always be closed, and thus the topological phase is not protected. At $k_2 = \pi$ and $k_2 = 2\pi$ the signal deviates from zero. For this special choice for k_2, the corresponding light shift matrix compensates itself.

$$\begin{pmatrix} e^{-ik_2} & 0 \\ 0 & e^{ik_2} \end{pmatrix} \begin{pmatrix} e^{-ik_2\sin(\theta)} & 0 \\ 0 & e^{ik_2\sin(\theta)} \end{pmatrix} \xrightarrow{k_2=\pi} \begin{pmatrix} -1 & 0 \\ 0 & -1 \end{pmatrix} \begin{pmatrix} e^{-ik_2\sin(\theta)} & 0 \\ 0 & e^{ik_2\sin(\theta)} \end{pmatrix} \qquad (77)$$

$$\begin{pmatrix} e^{-ik_2} & 0 \\ 0 & e^{ik_2} \end{pmatrix} \begin{pmatrix} e^{-ik_2\sin(\theta)} & 0 \\ 0 & e^{ik_2\sin(\theta)} \end{pmatrix} \xrightarrow{k_2=2\pi} \begin{pmatrix} 1 & 0 \\ 0 & 1 \end{pmatrix} \begin{pmatrix} e^{-ik_2\sin(\theta)} & 0 \\ 0 & e^{ik_2\sin(\theta)} \end{pmatrix} \qquad (78)$$

At $k_2 = \pi$ the compensation is perfect besides a factor of -1, while $k_2 = 2\pi$ unveils perfect compensation. Also note the region in configuration space for the fully compensated case, closely to $k_2 = 0$ with $\cos(K_1)\cos(K_2) \lesssim 1$. Within the simulations, a step on the first plateau has been observed. This region has been excluded from the fidelity, as described in Sec. 4.6.1. From this image one might conclude that this region is slightly unstable, causing this behavior.

Most importantly, the partially compensated case shows twice the amount of steps then expected before. Also, the jumps in the topological winding number are now only half as large. The convergence of the time-averaged MCD on the new topological steps is illustrated in B.6. However, if the light shift is indeed partially compensated one is able to predict and observe topological phase transitions.

5 Conclusion

5.1 Summary

Within this thesis, we have established a new interpretation for an already existing quantum walk experiment [4]. The existing discrepancies between theory and experiment could be settled by introducing a light shift induced alternative protocol, that might have been experimentally implemented. This new interpretation displayed characteristics of linearly evolving sidearms and the dominant center region, both observed in the experiment. By this new interpretation, the dominant center in the walk is explained by a rare combination of a walk protocol that is actually implemented with the $\hat{H}_2$ coin and a narrow initial ratchet state. Though rare, it is still plausible that exactly this might have happened in the experiment. Since a strong dependency of the fraction of the central region has been found on the size of the initial ratchet, this new theory would even be testable. The prediction is that for a larger ratchet the center region would naff off, while the original theory predicted that it would be independent of the initial ratchet size.

Also, further considerations on an experimental implementation of topological phase transitions in the double quantum kicked rotor have been made. Shortening the duration of the microwave rotations down to a quarter of the Talbot time demands manipulating the protocol, to construct a resonant configuration. This new protocol causes a change in sign within the topological phase curves that can be compensated by manipulating the microwave applications if desired. Also, the experimental effort could be reduced by only measuring either one internal state or independently of the internal states the joint momentum distribution. To do this, the discussed symmetries must be respected.

From investigations regarding the stability of the system, it is to say that the fluctuations in the complex phase of the microwave operator must be kept under sufficient control. If the fluctuations are adequately small, the topological steps stay visible. If they are however too large, the signal will not prevail. Also, exploiting the symmetry for measuring only one internal state does not indicate any significant disadvantage regarding the stability of the topological phase transitions.

Considering light-shift effects, it becomes clear that those have to be at least partially compensated. If they are indeed partially compensated as suggested, a topological signal is expected to be visible. However in this case the phase diagram for the winding number does change. Since this change can be predicted by the theory behind topological phase transitions in the double quantum kicked rotor, this would not pose a problem for the interpretation of the experimental data. In contrast it might even simplify the data taking, since a smaller parameter-window in k_2 would be sufficient to demonstrate topological phase transitions.
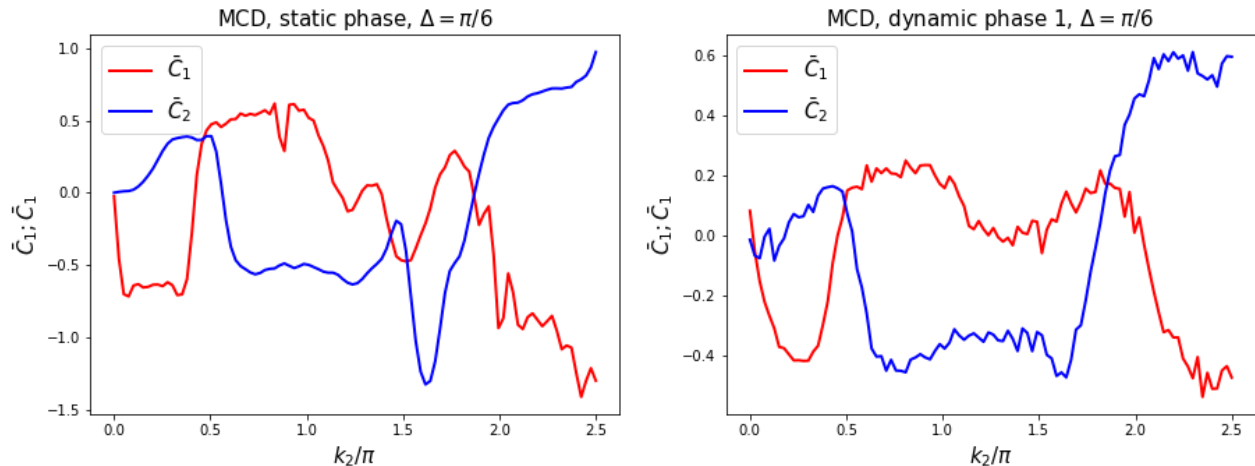
5.2 Outlook

Figure 14: Topological curves for 50 realizations of the Floquet implementation of the DQKR. Each MW rotation considers a free evolution of $\tau = \frac{4\pi}{6}$. The addition of a small amount of dynamic noise within the MW has stabilizing effects on the topological curves.

Within the process of finding an improved protocol for the double kicked quantum rotor, several possibilities for quasi-resonant protocols have been investigated. One idea was, that the one cycle of the evolution operators from Eq. (44) and Eq. (45) should correspond to a duration of a full Talbot period. Consequently, each microwave was assumed to have a duration of $\tau = \frac{4\pi}{6}$. Even though the topological curves were strongly disturbed, $\bar{C}_2$ from Fig. 14 experienced stabilization, as dynamic phase noise in for the MW was introduced. Too much noise destroyed the signal, just as before, but a sufficiently small amount had surprisingly stabilizing effects. Investigating this auto-stabilization could be an interesting subject for further theoretical research.

Ref. [5] discusses how the topological winding number connects to the number of protected $E = 0$ and $E = \pi$ energy states. From Fig. 13 it can be seen by comparing the ideal case with the case that considers partially compensated light shift effects, that within the range of $k_2 \in [0 : 2.5\pi]$ the configurations closing the bandgap are differently placed in configuration space, doubling the number of steps.
Returning to the underlying theory, it could be asked how the different placement of these $E = 0$ and $E = \pi$ states might be understood and whether the emergence of the factor 2 in the number of steps might be explained. From the connections between the „new" steps and the number of protected edge states, one might achieve a deeper understanding of the system.

Appendix

A Momentum distribution of kicked rotor walk with new walk protocol

A.1 Dependency on kick strength

In Ref. [30] it has been demonstrated that also for a different protocol an increase in the kick strength induces a peak in the center of the corresponding momentum distribution. This indicates that a dominant peak in the center might be typical behavior for strong dispersion in kicked-rotor walks. The current walk protocol appears to be rather susceptible to these effects since the peak is already observable at a rather small k as demonstrated in Fig. 15.
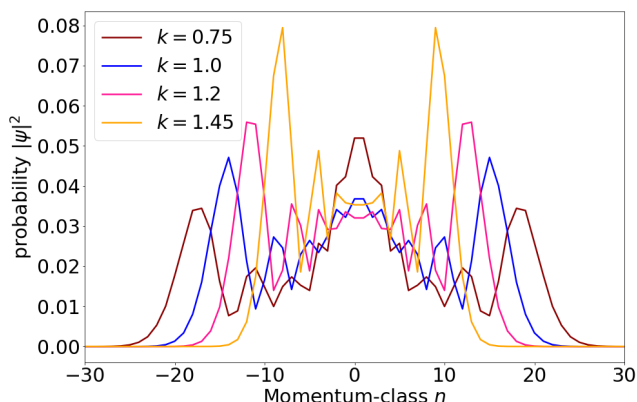

Figure 15: Shown are momentum distributions for QKR walks implemented by the $\hat{Y}$- gate and evolved with the $\hat{H}_2$-coin. It is demonstrated, that the peak in the center of the distribution becomes less prominent by lowering the kick strength k. This can be understood as an indicator that this behavior is caused by dispersion. The initial state is given by $|\psi_{in}\rangle = \frac{1}{2}|2\rangle \otimes (|n=0\rangle + i|n=1\rangle)$.

A.2 Analytical calculation of the momentum distribution

Following along the steps taken in Ref. [29] to obtain the momentum distribution for a similar walk protocol, we investigate in full detail the momentum distribution for the alternatively suggested walk protocol from Sec. 3.2.

A.2.1 Setup

One step in the quantum walk of interest is given by the evolution operator U. The walk will be initialized using the Y-matrix as the gate.

$$U = H_2 K = \frac{1}{\sqrt{2}} \begin{pmatrix} 1 & 1 \\ 1 & -1 \end{pmatrix} \begin{pmatrix} e^{-ik\cos(\theta)} & 0 \\ 0 & e^{ik\cos(\theta)} \end{pmatrix} \tag{79}$$

$$Y = \frac{1}{\sqrt{2}} \begin{pmatrix} 1 & i \\ i & 1 \end{pmatrix} \tag{80}$$

To solve for the evolution of the walk, one has to solve for U^T. With $N \equiv T - 1$ and $N \geq 0$. One defines U^T in the following fashion:

$$U^T = \left(\frac{1}{\sqrt{2}}\right)^T \begin{pmatrix} A_1^{(T-1)}(k) & A_2^{(T-1)}(k) \\ A_3^{(T-1)}(k) & A_4^{(T-1)}(k) \end{pmatrix}. \tag{81}$$

Repeating the steps of the calculation in Ref. [29], the ambition is to express the matrix elements as polynomials in the kick operator $e^{\pm ik\cos(\theta)}$ and then translate the resulting evolution back to momentum space.

Looking at the first few orders of the evolution, one notices that the matrix elements are related to each other by

$$A_1^{(N)}(k) = (-1)^{(N+1)} A_4^{(N)}(-k), \tag{82}$$

$$A_2^{(N)}(k) = (-1)^{(N+1)} A_3^{(N)}(-k). \tag{83}$$

The matrix entries will be found to be recursive polynomials. The initial conditions for those polynomials are

$$p_1^{(0)}(\tilde{z}) = p_2^{(0)}(\tilde{z}) = 1, \tag{84}$$

$$p_1^{(1)}(\tilde{z}) = z \equiv e^{-ik\cos(\theta)} + e^{ik\cos(\theta)}, \tag{85}$$

$$p_2^{(1)}(\tilde{z}) = \tilde{z} \equiv e^{-ik\cos(\theta)} - e^{ik\cos(\theta)}. \tag{86}$$

It is to be demonstrated by induction that the following equations for calculating the matrix elements hold for arbitrary N:

$$A_1^{(N)}(\tilde{z}) = e^{-ik\cos(\theta)} p_1^{(N)}(\tilde{z}) \tag{87}$$

$$A_2^{(N)}(\tilde{z}) = e^{ik\cos(\theta)} p_2^{(N)}(\tilde{z}), \tag{88}$$

where the polynomials $p_1^{(N)}$ and $p_2^{(N)}$ are defined by a recursion formula.

$$p^{(N)} = \tilde{z} p^{(N-1)} + 2 p^{(N-2)}. \tag{89}$$

It will be shown that the solution to the recursion can be written as polynomials in the kick operator, i.e.,

$$p_{1/2}^{(N)} = \sum_{l=0}^{N} a_{l,1/2} \, e^{ik\cos(\theta)(N-2l)}. \tag{90}$$

If one compares to Ref. [29], one should notice slight differences in the setup. The computations will be somewhat analogous, but will also show differences in the details. In this section, the matrix elements in Eq. (82) and Eq. (83) have different relations amongst each other. Also the polynomials in Eq. (84 - 86) are now functions in $\tilde{z}$ instead of having z. Slight deviations are also found in Eq. (87) and Eq. (88) and also the recursion formula shows the same structure but varies from the one reported in Ref. [29] for the walk with Y instead of H_2.

A.2.2 Solution to the recursion formula

Let us assume for now that Eq. (89) is true. To solve the equation one may choose the ansatz $p^{(N)}(z) \equiv x^N(z)$ and plug it in which yields

$$x^N = \tilde{z} x^{(N-1)} + 2 x^{(N-2)}. \tag{91}$$

This leads to a quadratic formula

$$x^2 = \tilde{z} x + 2, \tag{92}$$

with the solution

$$x_{1/2} = \frac{\tilde{z} \pm \sqrt{\tilde{z}^2 + 8}}{2}. \tag{93}$$

The recursion formula from above satisfies linearity. Therefore the general solution is given by a linear combination of both solutions.

$$p_{1/2}^{(N)}(z) = c_1 x_1^{(N)} + c_2 x_2^{(N)} \tag{94}$$

The coefficients c_1 and c_2 can be found by putting in the initial conditions which leads to

$$p_1^{(N)} = \frac{1}{2}\left(1 + \frac{2z - \tilde{z}}{\sqrt{\tilde{z}^2 + 8}}\right)\left(\frac{\tilde{z} + \sqrt{\tilde{z}^2 + 8}}{2}\right)^N + \frac{1}{2}\left(1 - \frac{2z - \tilde{z}}{\sqrt{\tilde{z}^2 + 8}}\right)\left(\frac{\tilde{z} - \sqrt{\tilde{z}^2 + 8}}{2}\right)^N \tag{95}$$

33

$$p_2^{(N)} = \frac{1}{2}\left(1 + \frac{\tilde{z}}{\sqrt{\tilde{z}^2 + 8}}\right)\left(\frac{\tilde{z} + \sqrt{\tilde{z}^2 + 8}}{2}\right)^N + \frac{1}{2}\left(1 - \frac{\tilde{z}}{\sqrt{\tilde{z}^2 + 8}}\right)\left(\frac{\tilde{z} - \sqrt{\tilde{z}^2 + 8}}{2}\right)^N. \tag{96}$$

Since the initial conditions and the recursion showed some differences from Ref. [29], we obtained a solution for the polynomials that differ in several signs and as stated above, the polynomials have their argument in $\tilde{z}$.

A.2.3 Prerequisites

Before continuing some simple relations will be shown that will later prove themselves to be useful:

$$
\begin{aligned}
z^2 - \tilde{z}^2 &= (e^{-ik\cos(\theta)} + e^{ik\cos(\theta)})^2 - (e^{-ik\cos(\theta)} - e^{ik\cos(\theta)})^2 \\
&= e^{-2ik\cos(\theta)} + e^{2ik\cos(\theta)} + 2 - (e^{-2ik\cos(\theta)} + e^{2ik\cos(\theta)} - 2) \\
&= 4
\end{aligned}
\tag{97}
$$

$$
\begin{aligned}
(z - \tilde{z})(z\tilde{z} + \tilde{z}^2 + 8) &= \left(e^{-ik\cos(\theta)} + e^{ik\cos(\theta)} - (e^{-ik\cos(\theta)} - e^{ik\cos(\theta)})\right) \\
&\quad \cdot \left((e^{-ik\cos(\theta)} + e^{ik\cos(\theta)})(e^{-ik\cos(\theta)} - e^{ik\cos(\theta)}) + (e^{-ik\cos(\theta)} - e^{ik\cos(\theta)})^2 + 8\right) \\
&= 2e^{ik\cos(\theta)}\left(e^{-2ik\cos(\theta)} - e^{2ik\cos(\theta)} + (e^{-2ik\cos(\theta)} + e^{2ik\cos(\theta)} - 2) + 8\right) \\
&= 2e^{ik\cos(\theta)}\left(2e^{-2ik\cos(\theta)} + 6\right) = 4\left(e^{-ik\cos(\theta)} + 3e^{ik\cos(\theta)}\right) \\
&= 4\left(2(e^{-ik\cos(\theta)} + e^{ik\cos(\theta)}) - 2(e^{-ik\cos(\theta)} - e^{ik\cos(\theta)})\right) \\
&= 4(2z - \tilde{z})
\end{aligned}
\tag{98}
$$

$$
\begin{aligned}
\tilde{z}^\alpha &= (e^{-ik\cos(\theta)} - e^{ik\cos(\theta)})^\alpha \\
&= \sum_{j=0}^{\alpha}\binom{\alpha}{j}(e^{-ik\cos(\theta)})^j(-e^{ik\cos(\theta)})^{\alpha-j} \\
&= \sum_{j=0}^{\alpha}\binom{\alpha}{j}(-1)^{\alpha-j}e^{ik\cos(\theta)(\alpha-2j)}
\end{aligned}
\tag{99}
$$

$$\int_0^{2\pi} e^{in\theta}e^{ik\cos\theta}d\theta = 2\pi i^n J_n(k) \tag{100}$$

$$J_{-a}(k) = (-1)^a J_a(k) \tag{101}$$

With Eq. (100) from Ref. [36].

A.2.4 Proof for recursion

We have already solved the recursion above by the ansatz. We still have to show that the solution of the recursion also solves for the matrix elements as stated in Eqs. (87) and (88). The proof will follow by induction. The statement is trivially true for $N = 0$, by the choice of the initial conditions. Now let the statement be true for N. Then we will show that the statement will also be true for $N + 1$. It is

$$U^{(T+1)} \propto \begin{pmatrix} A_1^{(T-1)}(k) & A_2^{(T-1)}(k) \\ A_3^{(T-1)}(k) & A_4^{(T-1)}(k) \end{pmatrix}\begin{pmatrix} e^{-ik\cos(\theta)} & e^{ik\cos(\theta)} \\ e^{-ik\cos(\theta)} & -e^{ik\cos(\theta)} \end{pmatrix}. \tag{102}$$

From that we can conclude:

$$A_1^{(N+1)} = e^{-ik\cos(\theta)}(A_1^{(N)} + A_2^{(N)}) \tag{103}$$

34

$$A_2^{(N+1)} = e^{ik\cos(\theta)}(A_1^{(N)} - A_2^{(N)}). \tag{104}$$

First we proof the induction for A_1.

$$A_1^{(N+1)} = e^{-ik\cos(\theta)}(A_1^{(N)} + A_2^{(N)}) \tag{105}$$

$$= e^{-ik\cos(\theta)}\left(e^{-ik\cos(\theta)}p_1^{(N)} + e^{ik\cos(\theta)}p_2^{(N)}\right) \tag{106}$$

$$= e^{-ik\cos(\theta)}\left(\frac{z+\tilde{z}}{2}p_1^{(N)} + \frac{z-\tilde{z}}{2}p_2^{(N)}\right) \tag{107}$$

$$= e^{-ik\cos(\theta)}\left(\tilde{z}p_1^{(N)} + \frac{z-\tilde{z}}{2}(p_1^{(N)} + p_2^{(N)})\right) \tag{108}$$

$$= e^{-ik\cos(\theta)}\left[\tilde{z}p_1^{(N)} + \frac{z-\tilde{z}}{2}\left(\frac{1}{2}\left(1+\frac{2z-\tilde{z}}{\sqrt{\tilde{z}^2+8}}\right)\left(\frac{\tilde{z}+\sqrt{\tilde{z}^2+8}}{2}\right)^N + \frac{1}{2}\left(1-\frac{2z-\tilde{z}}{\sqrt{\tilde{z}^2+8}}\right)\left(\frac{\tilde{z}-\sqrt{\tilde{z}^2+8}}{2}\right)^N\right.\right.$$
$$\left.\left.+\frac{1}{2}\left(1+\frac{\tilde{z}}{\sqrt{\tilde{z}^2+8}}\right)\left(\frac{\tilde{z}+\sqrt{\tilde{z}^2+8}}{2}\right)^N + \frac{1}{2}\left(1-\frac{\tilde{z}}{\sqrt{\tilde{z}^2+8}}\right)\left(\frac{\tilde{z}-\sqrt{\tilde{z}^2+8}}{2}\right)^N\right)\right] \tag{109}$$

$$= e^{-ik\cos(\theta)}\left[\tilde{z}p_1^{(N)} + \frac{z-\tilde{z}}{2}\left(\frac{1}{2}\left(2+\frac{2z}{\sqrt{\tilde{z}^2+8}}\right)\left(\frac{\tilde{z}+\sqrt{\tilde{z}^2+8}}{2}\right)^N + \frac{1}{2}\left(2-\frac{2z}{\sqrt{\tilde{z}^2+8}}\right)\left(\frac{\tilde{z}-\sqrt{\tilde{z}^2+8}}{2}\right)^N\right)\right] \tag{110}$$

$$= e^{-ik\cos(\theta)}\left[\tilde{z}p_1^{(N)} + \left(\left(\frac{z-\tilde{z}}{2}+\frac{z(z-\tilde{z})}{2\sqrt{\tilde{z}^2+8}}\right)\left(\frac{\tilde{z}+\sqrt{\tilde{z}^2+8}}{2}\right)^N\right.\right.$$
$$\left.\left.\left(\frac{z-\tilde{z}}{2}-+\frac{z(z-\tilde{z})}{2\sqrt{\tilde{z}^2+8}}\right)\left(\frac{\tilde{z}-\sqrt{\tilde{z}^2+8}}{2}\right)^N\right)\right] \tag{111}$$

$$= e^{-ik\cos(\theta)}\left[\tilde{z}p_1^{(N)} + \left(\frac{(z-\tilde{z}\tilde{z})}{4}+\frac{z\tilde{z}(z-\tilde{z})}{4\sqrt{\tilde{z}+8}}+\frac{\sqrt{\tilde{z}+8}(z-\tilde{z})}{4}+\frac{z(z-\tilde{z})}{4}\right)\left(\frac{\tilde{z}+\sqrt{\tilde{z}^2+8}}{2}\right)^{N-1}\right.$$
$$\left.+\left(\frac{(z-\tilde{z}\tilde{z})}{4}-\frac{z\tilde{z}(z-\tilde{z})}{4\sqrt{\tilde{z}+8}}-\frac{\sqrt{\tilde{z}+8}(z-\tilde{z})}{4}+\frac{z(z-\tilde{z})}{4}\right)\left(\frac{\tilde{z}-\sqrt{\tilde{z}^2+8}}{2}\right)^{N-1}\right] \tag{112}$$

$$= e^{-ik\cos(\theta)}\left[\tilde{z}p_1^{(N)} + \left(\frac{(z-\tilde{z})(z\tilde{z}+\tilde{z}^2+8)}{4\sqrt{\tilde{z}^2+8}}+\frac{z^2-\tilde{z}^2}{4}\right)\left(\frac{\tilde{z}+\sqrt{\tilde{z}^2+8}}{2}\right)^{N-1}\right.$$
$$\left.+\left(-\frac{(z-\tilde{z})(z\tilde{z}+\tilde{z}^2+8)}{4\sqrt{\tilde{z}^2+8}}+\frac{z^2-\tilde{z}^2}{4}\right)\left(\frac{\tilde{z}-\sqrt{\tilde{z}^2+8}}{2}\right)^{N-1}\right] \tag{113}$$

$$= e^{-ik\cos(\theta)}\left[\tilde{z}p_1^{(N)} + \left(1+\frac{2z-\tilde{z}}{\sqrt{\tilde{z}^2+8}}\right)\left(\frac{\tilde{z}+\sqrt{\tilde{z}^2+8}}{2}\right)^{N-1}+\left(1-\frac{2z-\tilde{z}}{\sqrt{\tilde{z}^2+8}}\right)\left(\frac{\tilde{z}-\sqrt{\tilde{z}^2+8}}{2}\right)^{N-1}\right] \tag{114}$$

$$= e^{-ik\cos(\theta)}\left[\tilde{z}p_1^{(N)} + 2p_1^{(N-1)}\right] \tag{115}$$

Therefore the induction for A_1 is complete. It remains to finish the induction for A_2.

$$A_2^{(N+1)} = e^{ik\cos(\theta)}(A_1^{(N)} - A_2^{(N)}) \tag{116}$$

$$= e^{ik\cos(\theta)} \left(e^{-ik\cos(\theta)} p_1^{(N)} - e^{ik\cos(\theta)} p_2^{(N)} \right) \tag{117}$$

$$= e^{ik\cos(\theta)} \left(\frac{z+\tilde{z}}{2} p_1^{(N)} - \frac{z-\tilde{z}}{2} p_2^{(N)} \right) \tag{118}$$

$$= e^{ik\cos(\theta)} \left(\tilde{z} p_2^{(N)} + \frac{z+\tilde{z}}{2} (p_1^{(N)} - p_2^{(N)}) \right) \tag{119}$$

$$= e^{ik\cos(\theta)} \left[\tilde{z} p_2^{(N)} + \frac{z+\tilde{z}}{2} \left(\frac{1}{2} \left(1 + \frac{2z-\tilde{z}}{\sqrt{\tilde{z}^2+8}} \right) \left(\frac{\tilde{z}+\sqrt{\tilde{z}^2+8}}{2} \right)^N + \frac{1}{2} \left(1 - \frac{2z-\tilde{z}}{\sqrt{\tilde{z}^2+8}} \right) \left(\frac{\tilde{z}-\sqrt{\tilde{z}^2+8}}{2} \right)^N \right. \right.$$
$$\left. \left. - \frac{1}{2} \left(1 + \frac{\tilde{z}}{\sqrt{\tilde{z}^2+8}} \right) \left(\frac{\tilde{z}+\sqrt{\tilde{z}^2+8}}{2} \right)^N - \frac{1}{2} \left(1 - \frac{\tilde{z}}{\sqrt{\tilde{z}^2+8}} \right) \left(\frac{\tilde{z}-\sqrt{\tilde{z}^2+8}}{2} \right)^N \right) \right] \tag{120}$$

$$= e^{ik\cos(\theta)} \left[\tilde{z} p_2^{(N)} + \frac{z+\tilde{z}}{2} \left(\frac{1}{2} \frac{(z-\tilde{z})}{\sqrt{\tilde{z}^2+8}} \left(\frac{\tilde{z}+\sqrt{\tilde{z}^2+8}}{2} \right)^N + \frac{1}{2} \frac{(-z+\tilde{z})}{\sqrt{\tilde{z}^2+8}} \left(\frac{\tilde{z}-\sqrt{\tilde{z}^2+8}}{2} \right)^N \right) \right] \tag{121}$$

$$= e^{ik\cos(\theta)} \left[\tilde{z} p_2^{(N)} + \frac{(z^2-\tilde{z}^2)}{2\sqrt{\tilde{z}^2+8}} \left(\frac{\tilde{z}+\sqrt{\tilde{z}^2+8}}{2} \right)^N + \frac{(\tilde{z}^2-z^2)}{2\sqrt{\tilde{z}^2+8}} \left(\frac{\tilde{z}-\sqrt{\tilde{z}^2+8}}{2} \right)^N \right] \tag{122}$$

$$= e^{ik\cos(\theta)} \left[\tilde{z} p_2^{(N)} + \left(\frac{\tilde{z}(z^2-\tilde{z}^2)}{4\sqrt{\tilde{z}^2+8}} + \frac{z^2-\tilde{z}^2}{4} \right) \left(\frac{\tilde{z}+\sqrt{\tilde{z}^2+8}}{2} \right)^{N-1} \right.$$
$$\left. + \left(\frac{\tilde{z}(z^2-\tilde{z}^2)}{4\sqrt{\tilde{z}^2+8}} - \frac{\tilde{z}^2-z^2}{4} \right) \left(\frac{\tilde{z}-\sqrt{\tilde{z}^2+8}}{2} \right)^{N-1} \right] \tag{123}$$

$$= e^{ik\cos(\theta)} \left[\tilde{z} p_2^{(N)} + \left(\frac{\tilde{z}}{\sqrt{\tilde{z}^2+8}} + 1 \right) \left(\frac{\tilde{z}+\sqrt{\tilde{z}^2+8}}{2} \right)^{N-1} + \left(-\frac{\tilde{z}}{\sqrt{\tilde{z}^2+8}} + 1 \right) \left(\frac{\tilde{z}-\sqrt{\tilde{z}^2+8}}{2} \right)^{N-1} \right] \tag{124}$$

$$= e^{ik\cos(\theta)} \left[\tilde{z} p_2^{(N)} + 2 p_2^{(N-1)} \right] \tag{125}$$

Therefore it is proofed that A_1 and A_2 follow the relations given above. A_3 and A_4 can from here on be calculated by (82) and (83).

A.2.5 Rewriting the polynomials

To obtain the final momentum distribution, it is convenient to rewrite the polynomials into a more accessible form. Therefore the polynomials will be rewritten into polynomials in the kick operator

$$p_1^N = \frac{1}{2} \left(1 + \frac{2z-\tilde{z}}{\sqrt{\tilde{z}^2+8}} \right) \left(\frac{\tilde{z}+\sqrt{\tilde{z}^2+8}}{2} \right)^N + \frac{1}{2} \left(1 - \frac{2z-\tilde{z}}{\sqrt{\tilde{z}^2+8}} \right) \left(\frac{\tilde{z}-\sqrt{\tilde{z}^2+8}}{2} \right)^N \tag{126}$$

$$= \frac{1}{2^{N+1}} \left[\left(1 + \frac{2z-\tilde{z}}{\sqrt{\tilde{z}^2+8}} \right) \left(\tilde{z}+\sqrt{\tilde{z}^2+8} \right)^N + \left(1 - \frac{2z-\tilde{z}}{\sqrt{\tilde{z}^2+8}} \right) \left(\tilde{z}-\sqrt{\tilde{z}^2+8} \right)^N \right] \tag{127}$$

$$= \frac{1}{2^{N+1}} \left[\left(\tilde{z}+\sqrt{\tilde{z}^2+8} \right)^N + \left(\tilde{z}-\sqrt{\tilde{z}^2+8} \right)^N + \frac{2z-\tilde{z}}{\sqrt{\tilde{z}^2+8}} \left(\left(\tilde{z}+\sqrt{\tilde{z}^2+8} \right)^N - \left(\tilde{z}-\sqrt{\tilde{z}^2+8} \right)^N \right) \right] \tag{128}$$

36

$$= \frac{1}{2^{N+1}} \left[\sum_{j=0}^{N} \binom{N}{j} \tilde{z}^{N-j} \left(\sqrt{\tilde{z}^2 + 8} \right)^j + \sum_{j=0}^{N} \binom{N}{j} \tilde{z}^{N-j} \left(-\sqrt{\tilde{z}^2 + 8} \right)^j \right.$$

$$\left. + \frac{2z - \tilde{z}}{\sqrt{\tilde{z}^2 + 8}} \left(\sum_{j=0}^{N} \binom{N}{j} \tilde{z}^{N-j} \left(\sqrt{\tilde{z}^2 + 8} \right)^j - \sum_{j=0}^{N} \binom{N}{j} \tilde{z}^{N-j} \left(-\sqrt{\tilde{z}^2 + 8} \right)^j \right) \right] \tag{129}$$

$$= \frac{1}{2^{N}} \left[\sum_{j=0}^{N/2} \binom{N}{2j} \tilde{z}^{N-2j} \left(\tilde{z}^2 + 8 \right)^j + \frac{2z - \tilde{z}}{\sqrt{\tilde{z}^2 + 8}} \left(\sum_{j=0}^{N/2} \binom{N}{2j+1} \tilde{z}^{N-2j-1} \left(\sqrt{\tilde{z}^2 + 8} \right)^{2j+1} \right) \right] \tag{130}$$

$$= \frac{1}{2^{N}} \left[\sum_{j=0}^{N/2} \left(\binom{N}{2j} - \binom{N}{2j+1} \right) \tilde{z}^{N-2j} \left(\tilde{z}^2 + 8 \right)^j + 2 \left(\sum_{j=0}^{N/2} \binom{N}{2j+1} z \tilde{z}^{N-2j-1} \left(\tilde{z}^2 + 8 \right)^j \right) \right] \tag{131}$$

$$= \frac{1}{2^{N}} \left[\sum_{j=0}^{N/2} \sum_{m=0}^{j} \left(\binom{N}{2j} - \binom{N}{2j+1} \right) \binom{j}{m} \tilde{z}^{N-2m} 8^m + 2 \sum_{j=0}^{N/2} \sum_{m=0}^{j} \binom{N}{2j+1} \binom{j}{m} z \tilde{z}^{N-2m-1} 8^m \right] \tag{132}$$

$$= \frac{1}{2^{N}} \left[\sum_{j=0}^{N/2} \sum_{m=0}^{j} \sum_{l=0}^{N-2m} \left(\binom{N}{2j} - \binom{N}{2j+1} \right) \binom{j}{m} \binom{N-2m}{l} (-1)^{N-2m-l} \cdot 8^m \cdot e^{ik\cos(\theta)(N-2m-2l)} \right]$$

$$+ \frac{1}{2^{N}} 2 \left[\sum_{j=0}^{N/2} \sum_{m=0}^{j} \sum_{l=0}^{N-2m-1} \binom{N}{2j+1} \binom{j}{m} \binom{N-2m-1}{l} (-1)^{N-2m-l-1} \cdot 8^m \cdot e^{ik\cos(\theta)(N-2m-2l-2)} \right]$$

$$+ \frac{1}{2^{N}} 2 \left[\sum_{j=0}^{N/2} \sum_{m=0}^{j} \sum_{l=0}^{N-2m-1} \binom{N}{2j+1} \binom{j}{m} \binom{N-2m-1}{l} (-1)^{N-2m-l-1} \cdot 8^m \cdot e^{ik\cos(\theta)(N-2m-2l)} \right] \tag{133}$$

$$= \frac{1}{2^{N}} \left[\sum_{j=0}^{N/2} \sum_{m=0}^{j} \sum_{l=0}^{N-2m} \left(\binom{N}{2j} - \binom{N}{2j+1} \right) \binom{j}{m} \binom{N-2m}{l} (-1)^{N-l} \cdot 8^m \cdot e^{ik\cos(\theta)(N-2m-2l)} \right]$$

$$- \frac{1}{2^{N}} 2 \left[\sum_{j=0}^{N/2} \sum_{m=0}^{j} \sum_{l=0}^{N-2m-1} \binom{N}{2j+1} \binom{j}{m} \binom{N-2m-1}{l} (-1)^{N-l} \cdot 8^m \cdot e^{ik\cos(\theta)(N-2m-2l-2)} \right]$$

$$- \frac{1}{2^{N}} 2 \left[\sum_{j=0}^{N/2} \sum_{m=0}^{j} \sum_{l=0}^{N-2m-1} \binom{N}{2j+1} \binom{j}{m} \binom{N-2m-1}{l} (-1)^{N-l} \cdot 8^m \cdot e^{ik\cos(\theta)(N-2m-2l)} \right] \tag{134}$$

$$= \sum_{l=0}^{N} a_{l,1} e^{ik\cos(\theta)(N-2l)} \tag{135}$$

Where in the last step one has changed indices from l to $l+m$. Note that for the upper part in (129) all odd powers cancel each other out, the same accounts for the uneven potencies of the lower part. Also one defined $a_{l,1}$ to be

$$a_{l,1} = \frac{1}{2^{N}} \sum_{j=0}^{N/2} \sum_{m=0}^{l} \left(\binom{N}{2j} - \binom{N}{2j+1} \right) \binom{j}{m} \binom{N-2m}{l-m} (-1)^{N-l+m} \cdot 8^m$$

$$+ \frac{1}{2^{N}} 2 \sum_{j=0}^{N/2} \sum_{m=0}^{l-1} \binom{N}{2j+1} \binom{j}{m} \binom{N-2m-1}{l-m-1} (-1)^{N-l+m} \cdot 8^m \tag{136}$$

$$- \frac{1}{2^{N}} 2 \sum_{j=0}^{N/2} \sum_{m=0}^{l} \binom{N}{2j+1} \binom{j}{m} \binom{N-2m-1}{l-m} (-1)^{N-l+m} \cdot 8^m.$$

Also note the factor (-1) dragged out in the third line of the coefficient $a_{l,1}$. That factor (-1) has a different reason in Ref. [29] since it is not resolved from the shift of the index. Analogous steps have to be taken for $p_2^{(N)}$.

$$p_2^{(N)} = \frac{1}{2}\left(1 + \frac{\tilde{z}}{\sqrt{\tilde{z}^2+8}}\right)\left(\frac{\tilde{z}+\sqrt{\tilde{z}^2+8}}{2}\right)^N + \frac{1}{2}\left(1 - \frac{\tilde{z}}{\sqrt{\tilde{z}^2+8}}\right)\left(\frac{\tilde{z}-\sqrt{\tilde{z}^2+8}}{2}\right)^N \tag{137}$$

$$= \frac{1}{2^{N+1}}\left[\left(1+\frac{\tilde{z}}{\sqrt{\tilde{z}^2+8}}\right)\left(\tilde{z}+\sqrt{\tilde{z}^2+8}\right)^N + \left(1-\frac{\tilde{z}}{\sqrt{\tilde{z}^2+8}}\right)\left(\tilde{z}-\sqrt{\tilde{z}^2+8}\right)^N\right] \tag{138}$$

$$= \frac{1}{2^{N+1}}\left[\left(\tilde{z}+\sqrt{\tilde{z}^2+8}\right)^N + \left(\tilde{z}-\sqrt{\tilde{z}^2+8}\right)^N + \frac{\tilde{z}}{\sqrt{\tilde{z}^2+8}}\left(\tilde{z}+\sqrt{\tilde{z}^2+8}\right)^N - \frac{\tilde{z}}{\sqrt{\tilde{z}^2+8}}\left(\tilde{z}-\sqrt{\tilde{z}^2+8}\right)^N\right] \tag{139}$$

$$= \frac{1}{2^{N+1}}\left[\sum_{j=0}^{N}\binom{N}{j}\tilde{z}^{N-j}\left(\sqrt{\tilde{z}^2+8}\right)^j + \sum_{j=0}^{N}\binom{N}{j}\tilde{z}^{N-j}\left(-\sqrt{\tilde{z}^2+8}\right)^j \right. $$
$$\left. + \frac{\tilde{z}}{\sqrt{\tilde{z}^2+8}}\left(\sum_{j=0}^{N}\binom{N}{j}\tilde{z}^{N-j}\left(\sqrt{\tilde{z}^2+8}\right)^j - \sum_{j=0}^{N}\binom{N}{j}\tilde{z}^{N-j}\left(-\sqrt{\tilde{z}^2+8}\right)^j\right)\right] \tag{140}$$

$$= \frac{1}{2^N}\left[\sum_{j=0}^{N/2}\binom{N}{2j}\tilde{z}^{N-2j}\left(\tilde{z}^2+8\right)^j + \frac{\tilde{z}}{\sqrt{\tilde{z}^2+8}}\sum_{j=0}^{N/2}\binom{N}{2j+1}\tilde{z}^{N-2j-1}\left(\sqrt{\tilde{z}^2+8}\right)^{2j+1}\right] \tag{141}$$

$$= \frac{1}{2^N}\left[\sum_{j=0}^{N/2}\binom{N}{2j}\tilde{z}^{N-2j}\left(\tilde{z}^2+8\right)^j + \sum_{j=0}^{N/2}\binom{N}{2j+1}\tilde{z}^{N-2j}\left(\tilde{z}^2+8\right)^j\right] \tag{142}$$

$$= \frac{1}{2^N}\left[\sum_{j=0}^{N/2}\binom{N+1}{2j+1}\tilde{z}^{N-2j}\left(\tilde{z}^2+8\right)^j\right] \tag{143}$$

$$= \frac{1}{2^N}\left[\sum_{j=0}^{N/2}\sum_{m=0}^{j}\binom{N+1}{2j+1}\binom{j}{m}\tilde{z}^{N-2m}8^m\right] \tag{144}$$

$$= \frac{1}{2^N}\left[\sum_{j=0}^{N/2}\sum_{m=0}^{j}\sum_{l=0}^{N-2m}\binom{N+1}{2j+1}\binom{j}{m}\binom{N-2m}{l}(-1)^{N-2m-l}\cdot 8^m \cdot e^{ik\cos(\theta)(N-2m-2l)}\right] \tag{145}$$

$$= \frac{1}{2^N}\left[\sum_{j=0}^{N/2}\sum_{m=0}^{j}\sum_{l=0}^{N-2m}\binom{N+1}{2j+1}\binom{j}{m}\binom{N-2m}{l}(-1)^{N-l}\cdot 8^m \cdot e^{ik\cos(\theta)(N-2m-2l)}\right] \tag{146}$$

$$= \frac{1}{2^N}\sum_{l=0}^{N}a_{l,2}\cdot e^{ik\cos(\theta)(N-2l)} \tag{147}$$

Again in the last step the index l has been shifted to $l+m$ and $a_{l,2}$ has been defined to be:

$$a_{l,2} = \frac{1}{2^N}\sum_{j=0}^{N/2}\sum_{m=0}^{l}\binom{N+1}{2j+1}\binom{j}{m}\binom{N-2m}{l-m}(-1)^{N-l+m}\cdot 8^m \tag{148}$$

Please note that in (136) and (148) the factor $(-1)^N$ is a global factor and therefore irrelevant.

A.2.6 Obtaining the momentum-distribution

Since the intention is to implement a ratchet state consider Eq. (18). As already stated above, the ratchet state is initialized by the application of the beamsplitter matrix $\hat{Y}$. We organise our internal basis $|1\rangle \equiv \binom{0}{1}$

and $|2\rangle \equiv \binom{1}{0}$. Therefore the total initial state is given by

$$\psi_{in} = \frac{1}{\sqrt{2}} \left(i|1\rangle + |2\rangle \right) \otimes \frac{1}{\sqrt{S}} \sum_s e^{-is\frac{\pi}{2}} |n = s\rangle. \tag{149}$$

The total momentum distribution is given as the sum of the momentum distributions of both the respective internal states.

$$P(n,T) = P_{|1\rangle}(n,T) + P_{|2\rangle}(n,T) \tag{150}$$

$$= \left[\left| \frac{1}{\sqrt{2\pi}} \int_0^{2\pi} e^{-in\theta} \langle \theta, 1| U^T |\psi_{in}\rangle d\theta \right|^2 + \left| \frac{1}{\sqrt{2\pi}} \int_0^{2\pi} e^{-in\theta} \langle \theta, 2| U^T |\psi_{in}\rangle d\theta \right|^2 \right] \tag{151}$$

$$= \left[\left| \frac{1}{\sqrt{2\pi}} \int_0^{2\pi} e^{-in\theta} \left(\frac{1}{\sqrt{2}} \right)^T \langle \theta, 1| \begin{pmatrix} A_1^{(T-1)}(k) & A_2^{(T-1)}(k) \\ A_3^{(T-1)}(k) & A_4^{(T-1)}(k) \end{pmatrix} \frac{1}{\sqrt{2}} \left(i|1\rangle + |2\rangle \right) \otimes \frac{1}{\sqrt{S}} \sum_s e^{-is\frac{\pi}{2}} |n = s\rangle \right|^2 \right.$$

$$\left. + \left| \frac{1}{\sqrt{2\pi}} \int_0^{2\pi} e^{-in\theta} \left(\frac{1}{\sqrt{2}} \right)^T \langle \theta, 2| \begin{pmatrix} A_1^{(T-1)}(k) & A_2^{(T-1)}(k) \\ A_3^{(T-1)}(k) & A_4^{(T-1)}(k) \end{pmatrix} \frac{1}{\sqrt{2}} \left(i|1\rangle + |2\rangle \right) \otimes \frac{1}{\sqrt{S}} \sum_s e^{-is\frac{\pi}{2}} |n = s\rangle \right|^2 \right] \tag{152}$$

$$= \frac{1}{2^{T+1}S} \left[\left| \frac{1}{\sqrt{2\pi}} \int_0^{2\pi} e^{-in\theta} \left(iA_1^{(T-1)} + A_2^{(T-1)} \right) \sum_s (-i)^s \langle \theta | n = s\rangle d\theta \right|^2 \right.$$

$$\left. + \left| \frac{1}{\sqrt{2\pi}} \int_0^{2\pi} e^{-in\theta} \left(iA_3^{(T-1)} + A_4^{(T-1)} \right) \sum_s (-i)^s \langle \theta | n = s\rangle d\theta \right|^2 \right] \tag{153}$$

$$= \frac{1}{2^{T+1}S} \left[\left| \frac{1}{2\pi} \int_0^{2\pi} e^{-in\theta} \left(iA_1^{(T-1)} + A_2^{(T-1)} \right) \sum_s (-i)^s e^{is\theta} d\theta \right|^2 \right.$$

$$\left. + \left| \frac{1}{2\pi} \int_0^{2\pi} e^{-in\theta} \left(iA_3^{(T-1)} + A_4^{(T-1)} \right) \sum_s (-i)^s e^{is\theta} d\theta \right|^2 \right] \tag{154}$$

$$= \frac{1}{2^{T+1}S} \left[\left| \frac{1}{2\pi} \int_0^{2\pi} \sum_s (-i)^s e^{-i(n-s)\theta} \left(i \sum_{l=0}^N a_{l,1} e^{ik\cos\theta(N-2l-1)} + \sum_{l=0}^N a_{l,2} e^{ik\cos\theta(N-2l+1)} \right) d\theta \right|^2 \right.$$

$$\left. + \left| \frac{1}{2\pi} \int_0^{2\pi} \sum_s (-i)^s e^{-i(n-s)\theta} \left(i \sum_{l=0}^N (-1)^N a_{l,1} e^{-ik\cos\theta(N-2l-1)} + \sum_{l=0}^N (-1)^{N+1} a_{l,2} e^{-ik\cos\theta(N-2l+1)} \right) d\theta \right|^2 \right] \tag{155}$$

$$= \frac{1}{2^{T+1}S} \left[\left| i \sum_{l=0}^N \sum_s a_{l,1} (-i)^s i^{-(n-s)} J_{-(n-s)} \left((N-2l-1)k \right) \right. \right.$$

$$\left. + \sum_{l=0}^N \sum_s a_{l,2} (-i)^s i^{-(n-s)} J_{-(n-s)} \left((N-2l+1)k \right) \right|^2$$

$$+ \left| i \sum_{l=0}^N \sum_s a_{l,1} (-1)^N (-i)^s i^{-(n-s)} J_{-(n-s)} \left(-(N-2l-1)k \right) \right.$$

$$\left. \left. + \sum_{l=0}^N \sum_s a_{l,2} (-1)^{N+1} (-i)^s i^{-(n-s)} J_{-(n-s)} \left(-(N-2l+1)k \right) \right|^2 \right] \tag{156}$$

$$= \frac{1}{2^{T+1}S} \left[\left| i \sum_{l=0}^{N} \sum_{s} a_{l,1}(-1)^{(n-s)} J_{(n-s)} \left((N-2l-1)k \right) + \sum_{l=0}^{N} \sum_{s} a_{l,2}(-1)^{(n-s)} J_{(n-s)} \left((N-2l+1)k \right) \right|^2 \right.$$

$$\left. + \left| i \sum_{l=0}^{N} \sum_{s} a_{l,1}(-1)^{(n-s)} J_{(n-s)} \left(-(N-2l-1)k \right) + \sum_{l=0}^{N} \sum_{s} a_{l,2}(-1)^{(n-s)} J_{(n-s)} \left(-(N-2l+1)k \right) \right|^2 \right] \tag{157}$$

$$= \frac{1}{2^{T+1}S} \left[\left(\sum_{l=0}^{N} \sum_{s} a_{l,1}(-1)^{s} J_{(n-s)} \left((N-2l-1)k \right) \right)^2 + \left(\sum_{l=0}^{N} \sum_{s} a_{l,2}(-1)^{s} J_{(n-s)} \left((N-2l+1)k \right) \right)^2 + \right.$$

$$\left. \left(\sum_{l=0}^{N} \sum_{s} a_{l,1}(-1)^{s} J_{(n-s)} \left(-(N-2l-1)k \right) \right)^2 + \left(\sum_{l=0}^{N} \sum_{s} a_{l,2}(-1)^{s} J_{(n-s)} \left(-(N-2l+1)k \right) \right)^2 \right]. \tag{158}$$

Even though the computation shows variations in its details, the momentum distributions found in Eq. (158) and in Ref. [29] are of the same analytical form. Nevertheless, the coefficients $a_{l,1}$ and $a_{l,2}$ differ from each other.

B   Background considerations on investigations regarding the DQKR system

B.1   rewriting chiral symmetric operators

The following calculation intends to rewrite the kicks in the evolution operator into an experimentally applicable form. This section's purpose is to avoid secondary confusion by presenting a full calculation for both kick-operators, highlighting the error made in Ref. [6, 28] as it appears.

The Pauli matrices are given for reasons of brevity below.

$$\sigma_x = \begin{pmatrix} 0 & 1 \\ 1 & 0 \end{pmatrix} \qquad \sigma_y = \begin{pmatrix} 0 & -i \\ i & 0 \end{pmatrix} \qquad \sigma_z = \begin{pmatrix} 1 & 0 \\ 0 & -1 \end{pmatrix} \tag{159}$$

Using $\sigma_j^2 = \mathbf{1}$ it follows simply by Taylor-expansion:

$$e^{-iX\sigma_j} = \cos(X)\mathbf{1} - i\sin(X)\sigma_j \tag{160}$$

With X being an arbitrary variable for now. With that relation one finds for the different Pauli-matrices expressions to rewrite the exponential.

$$e^{-iX\sigma_x} = \begin{pmatrix} \cos(X) & -i\sin(X) \\ -i\sin(X) & \cos(X) \end{pmatrix} \qquad e^{-iX\sigma_y} = \begin{pmatrix} \cos(X) & -\sin(X) \\ \sin(X) & \cos(X) \end{pmatrix} \qquad e^{-iX\sigma_z} = \begin{pmatrix} e^{-iX} & 0 \\ 0 & e^{iX} \end{pmatrix} \tag{161}$$

Therefore we can write:

$$\hat{M}(-\frac{\pi}{2},0)e^{-iK\sigma_z}\hat{M}(\frac{\pi}{2},0) = \begin{pmatrix} \cos(\frac{\pi}{4}) & -\sin(\frac{\pi}{4}) \\ \sin(\frac{\pi}{4}) & \cos(\frac{\pi}{4}) \end{pmatrix} \begin{pmatrix} e^{-iK} & 0 \\ 0 & e^{iK} \end{pmatrix} \begin{pmatrix} \cos(\frac{\pi}{4}) & \sin(\frac{\pi}{4}) \\ -\sin(\frac{\pi}{4}) & \cos(\frac{\pi}{4}) \end{pmatrix} \tag{162}$$

$$= \frac{1}{2} \begin{pmatrix} 1 & -1 \\ 1 & 1 \end{pmatrix} \begin{pmatrix} e^{-iK} & 0 \\ 0 & e^{iK} \end{pmatrix} \begin{pmatrix} 1 & 1 \\ -1 & 1 \end{pmatrix} \tag{163}$$

$$= \frac{1}{2} \begin{pmatrix} 1 & -1 \\ 1 & 1 \end{pmatrix} \begin{pmatrix} e^{-iK} & e^{-iK} \\ -e^{iK} & e^{iK} \end{pmatrix} \tag{164}$$

$$= \frac{1}{2} \begin{pmatrix} e^{-iK} + e^{iK} & e^{-iK} - e^{iK} \\ e^{-iK} - e^{iK} & e^{-iK} + e^{iK} \end{pmatrix} \tag{165}$$

$$= \begin{pmatrix} \cos(K) & -i\sin(K) \\ -i\sin(K) & \cos(K) \end{pmatrix} = e^{-iK\sigma_x} \tag{166}$$

With $\hat{M}(\alpha, \chi)$ from Eq. (12). Therefore we can write:

$$e^{-iK\sigma_x} = e^{-i\frac{\pi}{4}\sigma_y}e^{-iK\sigma_z}e^{i\frac{\pi}{4}\sigma_y} = \hat{M}(-\frac{\pi}{2}, 0)e^{-iK\sigma_z}\hat{M}(\frac{\pi}{2}, 0) \tag{167}$$

However in the Ref. [6, 28]:

$$e^{-iK\sigma_x} = e^{i\frac{\pi}{4}\sigma_y}e^{-iK\sigma_z}e^{-i\frac{\pi}{4}\sigma_y} = \hat{M}(-\frac{\pi}{2}, 0)e^{-iK\sigma_z}\hat{M}(\frac{\pi}{2}, 0) \tag{168}$$

For the sake of completeness we can repeat the same calculation for the kick in y-direction.

$$\hat{M}(-\frac{\pi}{2}, \frac{\pi}{2})e^{-iK\sigma_z}\hat{M}(\frac{\pi}{2}, \frac{\pi}{2}) = \begin{pmatrix} cos(\frac{\pi}{4}) & i\ sin(\frac{\pi}{4}) \\ i\ sin(\frac{\pi}{4}) & cos(\frac{\pi}{4}) \end{pmatrix} \begin{pmatrix} e^{-iK} & 0 \\ 0 & e^{iK} \end{pmatrix} \begin{pmatrix} cos(\frac{\pi}{4}) & -i\ sin(\frac{\pi}{4}) \\ -i\ sin(\frac{\pi}{4}) & cos(\frac{\pi}{4}) \end{pmatrix} \tag{169}$$

$$= \frac{1}{2}\begin{pmatrix} 1 & i \\ i & 1 \end{pmatrix}\begin{pmatrix} e^{-iK} & 0 \\ 0 & e^{iK} \end{pmatrix}\begin{pmatrix} 1 & -i \\ -i & 1 \end{pmatrix} \tag{170}$$

$$= \frac{1}{2}\begin{pmatrix} 1 & i \\ i & 1 \end{pmatrix}\begin{pmatrix} e^{-iK} & -i\ e^{-iK} \\ -i\ e^{iK} & e^{iK} \end{pmatrix} \tag{171}$$

$$= \frac{1}{2}\begin{pmatrix} e^{-iK} + e^{iK} & -i\ (e^{-iK} - e^{iK}) \\ i\ (e^{-iK} - e^{iK}) & e^{-iK} + e^{iK} \end{pmatrix} \tag{172}$$

$$= \begin{pmatrix} cos(K) & -sin(K) \\ sin(K) & cos(K) \end{pmatrix} = e^{-iK\sigma_y} \tag{173}$$

$$\Rightarrow e^{-iK\sigma_y} = e^{i\frac{\pi}{4}\sigma_x}e^{-iK\sigma_z}e^{-i\frac{\pi}{4}\sigma_x} = \hat{M}(-\frac{\pi}{2}, \frac{\pi}{2})e^{-iK\sigma_z}\hat{M}(\frac{\pi}{2}, \frac{\pi}{2}) \tag{174}$$

Just as stated in the Ref. [28].

B.2   Prerequisites for protocol resonance considerations

First let us consider the free evolution operator $\hat{P} = e^{-i\frac{(\hat{n}+\beta)^2}{2}\tau}$, with for a quarter Talbot time $\tau = \pi$ and neglecting quassimomentum $\beta = 0$. It is trivially true that when an integer number n is even, then the square of the number is also even. The same conclusion can be drawn for uneven numbers. Under this consideration, we can identify similarly to Ref. [28] the free evolution operator with the shift operator in local space.

$$P_\pi^2 = (e^{-i\frac{n^2}{2}\pi})^2 = e^{-in^2\pi} = \begin{cases} 1 & n = 2j \\ -1 & n = 2j+1 \end{cases} \equiv e^{-in\pi} \equiv T(\pi) \tag{175}$$

From here $\hat{T}(\pi)$ will denote the shift operator in angular momentum space for $\theta = \pi$
Please note the following relations:

1) The following MW-applications correspond to inverse rotations:

$$M(\frac{\pi}{2}, 0) = M(-\frac{\pi}{2}, 0)^{-1} \tag{176}$$

$$M(-\frac{\pi}{2}, \frac{\pi}{2}) = M(\frac{\pi}{2}, \frac{\pi}{2})^{-1} \tag{177}$$

2) The free evolution operator for the two-state system commutes with the microwaves since the entries of the MW-matrix are scalar values.

$$\hat{P} = e^{-i\frac{(\hat{n}+\beta)^2}{2}\tau\otimes\mathbf{1}} = e^{-i\frac{(\hat{n}+\beta)^2}{2}\tau} \cdot \mathbf{1} \tag{178}$$

$$\Rightarrow \hat{P}\hat{M}(\alpha_1, \chi_1)\hat{P}\hat{M}(\alpha_2, \chi_2) = \hat{M}(\alpha_1, \chi_1)\hat{M}(\alpha_2, \chi_2)\hat{P}^2 \tag{179}$$

$$= \hat{M}(\alpha_1, \chi_1)\hat{M}(\alpha_2, \chi_2)\hat{T}(\pi) \tag{180}$$

3) Consider how the translation operator affects the kick operators $\hat{K}_1$ and $\hat{K}_2$:

$$\hat{T}(\pi)\hat{K}_{1,2}(k, \theta) = \hat{K}_{1,2}(k, \theta + \pi) = \hat{K}_{1,2}(-k, \theta) \equiv \hat{K}_{1,2}^{-1} \tag{181}$$

$$\hat{T}(2\pi)\hat{K}_{1,2}(k, \theta) = \hat{K}_{1,2}(k, \theta + 2\pi) = \hat{K}_{1,2}(k, \theta) \tag{182}$$

B.3 Local properties

Consider the sequence $P(\beta = 0, \tau = \pi)_n = e^{-i\frac{n^2}{2}\pi} = (-i)^{n^2}$. It will be proofed by induction that the following is true:

$$\text{1) if } n = 2j \rightarrow (-i)^{n^2} = 1 \tag{183}$$

$$\text{2) if } n = 2j + 1 \rightarrow (-i)^{n^2} = -i \tag{184}$$

The induction will be shown over the integer j. To show 1) Let n be even. The statement is trivially true for $j = 0$. So now let the statement above be true for $j - 1$. It is $j^2 = (j-1)^2 + 2j - 1$. For $n = 2j$ we can therefore compute $n^2 = 4j^2 = 4(j-1)^2 + 8j - 4$. Thus we can conclude:

$$(-i)^{n^2} = (-i)^{4(j-1)^2 + 8j - 4} = (-i^{4(j-1)^2}(-i)^{8j}(-i)^4 = (-i)^{4(j-1)^2} = 1^{(j-1)^2} = 1 \tag{185}$$

It remains to show the induction for 2). So let n be odd. Again the statement follows trivially for $j = 0$, so let the statement be true for $j - 1$. Analogously to above we find: $n^2 = (2j)^2 + 4j + 1$. Therefore:

$$(-i)^{n^2} = (-i)^{(2j)^2 + 4j + 1} = (-i)^{(2j)^2}(-i)^{4j}(-i) = -i \tag{186}$$

In the last step we have used the result from 1) and $(-i)^{4j} = 1$.

From above we conclude that $\hat{P}_\pi \neq e^{-i\frac{\hat{n}}{2}\pi}$, so $\hat{P}_\pi$ can not casually be identified with the translation operator in local space. Yet, within the operators $\hat{U}_1$ and $\hat{U}_2$ the MWs and thus indirectly free evolutions always appear in pairs. Therefore it is still possible within our specific configuration to identify $\hat{P}(\beta = 0, \tau = \pi)$ with the translation operator $\hat{T}(\frac{\pi}{2}) \equiv e^{-i\frac{\hat{n}}{2}\pi}$.

B.4 Compensation of sign

As a consequence of the resonant protocol, the kick-lattice structure is flipped in local space. Therefore the evolution of the wave functions of the internal states is mirrored and the MCD experiences a change in sign. By changing the MW configuration in the protocol, the orientation of the kick-lattice can be changed again back to its original orientation. This way the change in sign in the MCD can be compensated.

$$\hat{M}(-\frac{\pi}{2}, 0)e^{-ik_1\cos(\hat{\theta})\sigma_z}\hat{M}(\frac{\pi}{2}, 0) = \begin{pmatrix} cos(\frac{\pi}{4}) & -sin(\frac{\pi}{4}) \\ sin(\frac{\pi}{4}) & cos(\frac{\pi}{4}) \end{pmatrix} \begin{pmatrix} e^{-ik_1\cos(\hat{\theta})} & 0 \\ 0 & e^{ik_1\cos(\hat{\theta})} \end{pmatrix} \begin{pmatrix} cos(\frac{\pi}{4}) & sin(\frac{\pi}{4}) \\ -sin(\frac{\pi}{4}) & cos(\frac{\pi}{4}) \end{pmatrix} \tag{187}$$

$$= \frac{1}{2} \begin{pmatrix} 1 & -1 \\ 1 & 1 \end{pmatrix} \begin{pmatrix} e^{-ik_1\cos(\hat{\theta})} & 0 \\ 0 & e^{ik_1\cos(\hat{\theta})} \end{pmatrix} \begin{pmatrix} 1 & 1 \\ -1 & 1 \end{pmatrix} \tag{188}$$

$$= \frac{1}{2} \begin{pmatrix} 1 & -1 \\ 1 & 1 \end{pmatrix} \begin{pmatrix} e^{-ik_1\cos(\hat{\theta})} & e^{-ik_1\cos(\hat{\theta})} \\ -e^{ik_1\cos(\hat{\theta})} & e^{ik_1\cos(\hat{\theta})} \end{pmatrix} \tag{189}$$

$$= \frac{1}{2} \begin{pmatrix} e^{-ik_1\cos(\hat{\theta})} + e^{ik_1\cos(\hat{\theta})} & e^{-ik_1\cos(\hat{\theta})} - e^{ik_1\cos(\hat{\theta})} \\ e^{-ik_1\cos(\hat{\theta})} - e^{ik_1\cos(\hat{\theta})} & e^{-ik_1\cos(\hat{\theta})} + e^{ik_1\cos(\hat{\theta})} \end{pmatrix} \tag{190}$$

$$= \frac{1}{2} \begin{pmatrix} 1 & 1 \\ -1 & 1 \end{pmatrix} \begin{pmatrix} e^{ik_1\cos(\hat{\theta})} & -e^{ik_1\cos(\hat{\theta})} \\ e^{-ik_1\cos(\hat{\theta})} & e^{-ik_1\cos(\hat{\theta})} \end{pmatrix} \tag{191}$$

$$= \frac{1}{2} \begin{pmatrix} 1 & 1 \\ -1 & 1 \end{pmatrix} \begin{pmatrix} e^{ik_1\cos(\hat{\theta})} & 0 \\ 0 & e^{-ik_1\cos(\hat{\theta})} \end{pmatrix} \begin{pmatrix} 1 & -1 \\ 1 & 1 \end{pmatrix} \tag{192}$$

$$= \begin{pmatrix} cos(\frac{\pi}{4}) & sin(\frac{\pi}{4}) \\ -sin(\frac{\pi}{4}) & cos(\frac{\pi}{4}) \end{pmatrix} \begin{pmatrix} e^{ik_1\cos(\hat{\theta})} & 0 \\ 0 & e^{-ik_1\cos(\hat{\theta})} \end{pmatrix} \begin{pmatrix} cos(\frac{\pi}{4}) & -sin(\frac{\pi}{4}) \\ sin(\frac{\pi}{4}) & cos(\frac{\pi}{4}) \end{pmatrix} \tag{193}$$

$$= \hat{M}(\frac{\pi}{2}, 0)e^{ik_1\cos(\hat{\theta})\sigma_z}\hat{M}(-\frac{\pi}{2}, 0) \tag{194}$$

B.5   Simulations

Simulating three different models for fluctuations in χ, the stability of the topological phase transitions under these fluctuations is investigated. The simulations calculating the MCD from both internal states are presented in Sec. 4.6.2. The symmetry from Sec. 4.5 allows for either measuring only one internal state or measuring the joint momentum distribution. Within this section, more detailed investigations are presented on the stability of the topological phase transitions, if this symmetry is exploited.
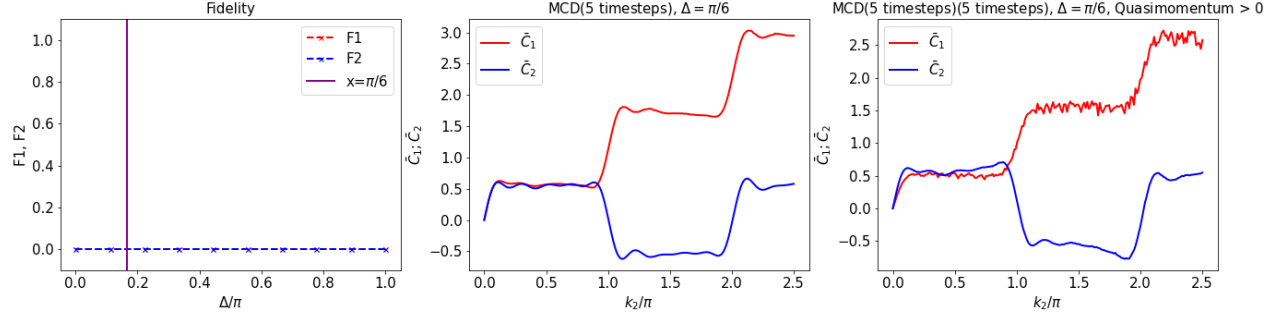

Figure 16: Implementation of Model 1. The fidelity shows a weak dependency on the range of phase fluctuations Δ. The exemplary image at $\Delta = \frac{\pi}{6}$ is close to the ideal case for 5 steps in the evolution. It is seen that quasimomentum is distorting the steps slightly stronger compared to Fig. 9. The simulation is implemented for 1000 realizations and one internal state is measured to compute the MCD, exploiting the symmetry from Sec. 4.5. The initial state is given by $|\psi_{in}\rangle = |2\rangle \otimes |n = 0\rangle)$.
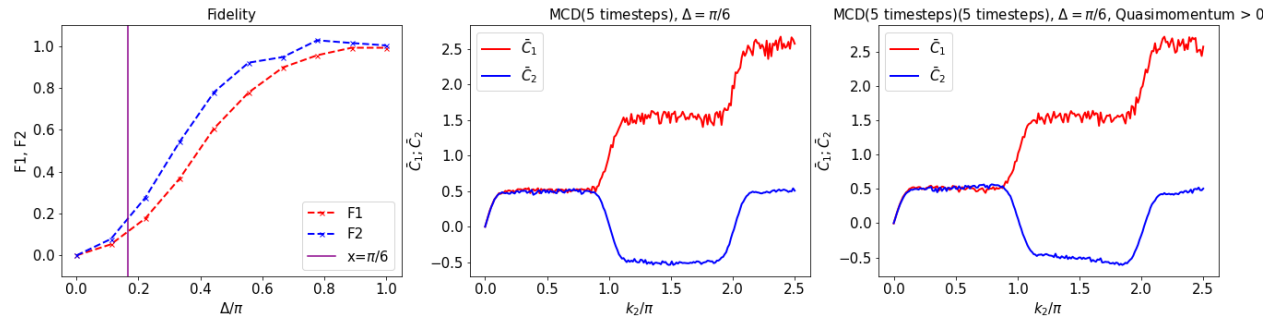

Figure 17: Implementation of Model 2. The fidelity shows a strong dependency on the range of phase fluctuations Δ. The exemplary image at $\Delta = \frac{\pi}{6}$ shows already some perturbations within the topological curve, while the steps stay well visible. The impact of quasimomentum leads to some additional deformation but does not pose a great threat to the „survival " of the steps, as long the phase noise within the MW is controlled. The simulation is implemented for 1000 realizations and one internal state is measured to compute the MCD, exploiting the symmetry from Sec. 4.5. The initial state is given by $|\psi_{in}\rangle = |2\rangle \otimes |n = 0\rangle$.
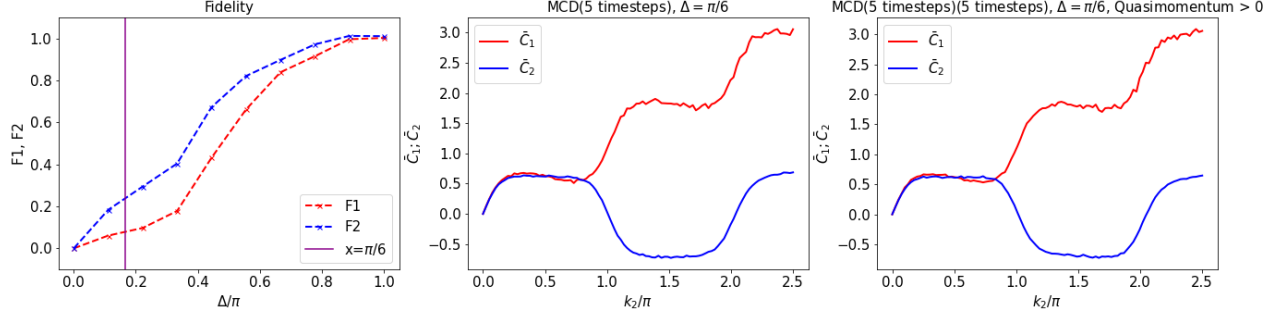
Figure 18: Implementation of Model 3. The fidelity shows a strong dependency on the range length of the steps within the phase drift, dependent on Δ. The exemplary image at $\Delta = \frac{\pi}{6}$ shows already some deformations within the topological curve. The steps stay well visible, but the phase transition is not as sharp as in model 1 and model 2. above. The impact of quasimomentum does not significantly contribute to the deformation of the curve. The simulation is implemented for 1000 realizations and one internal state is measured to compute the MCD, exploiting the symmetry from Sec. 4.5. The initial state is given by $|\psi_{in}\rangle = |2\rangle \otimes |n = 0\rangle$.
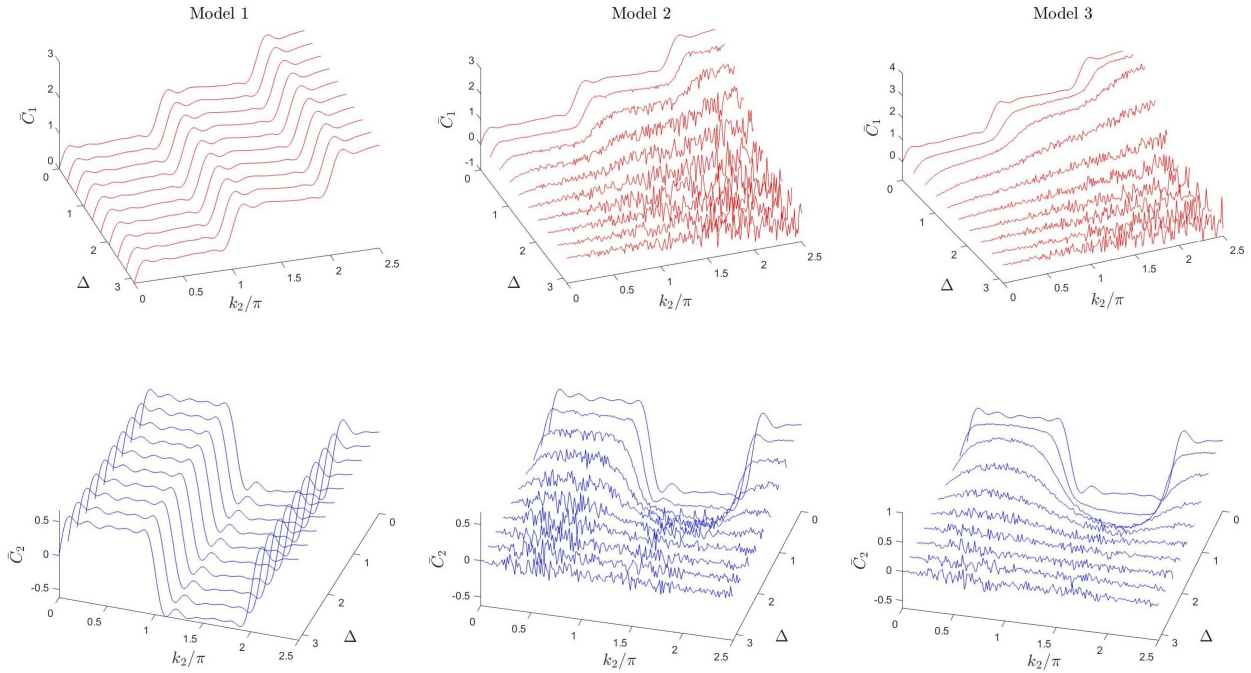

Figure 19: Implementation of the different phase noise models. Shown is the impact of perturbance $\Delta \in [0; \pi]$ on the topological curves. The MCD is averaged over five applications of the evolution operator. As suggested by the fidelity curves the dynamic models (2) and (3) show strong signal decay for increasing Δ. The static model (1) shows a very weak dependency on Δ. Exploiting the symmetry from Sec. 4.5, the momentum distribution is not measured for one internal state specifically, but $P(t) = P(t)_{|1\rangle} + P(t)_{|2\rangle}$. The simulations are implemented for 1000 realisations and the initial state is given by $|\psi_{in}\rangle = |2\rangle \otimes |n = 0\rangle$.

B.6   Light shift compensation

If light-shift effects are introduced, the topological signal is predicted to decay. If they are again partially compensated, as suggested in Sec. 1.2.4, topological steps are visible again but they deviate from the ideal case. Fig. 20 demonstrates the convergence of the time-averaged mean chiral displacement on the steps predicted by the underlying theory. The bottom line is that also for the new configuration the MCD converges onto the topological steps. That means in principle this configuration could be experimentally observed.
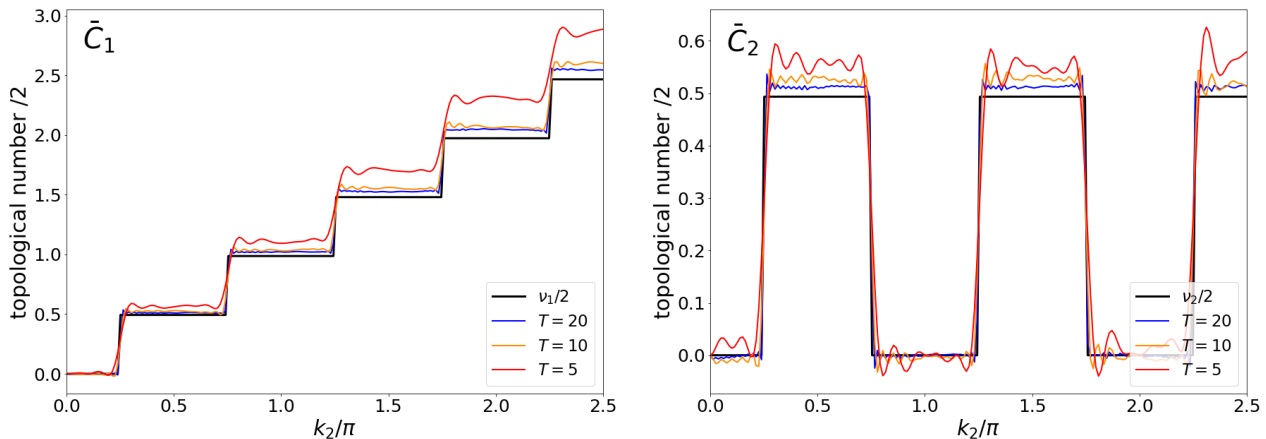

Figure 20: Illustrated is the convergence of the time-averaged MCD for the chiral symmetric evolution operators $\hat{U}_1$ and $\hat{U}_2$ for the partially light shift compensated case. The theoretical curves calculated by Eq. (21) are represented in black. For five applications of the evolution operator, the steps are already quite well visible, even though deviations seem to become stronger at higher values for the topological number. Better convergence is achieved at higher time steps.

References

[1] J Kempe. Quantum random walks: An introductory overview. *Contemporary Physics*, 44(4):307–327, Jul 2003.

[2] J M Kosterlitz and D J Thouless. Ordering, metastability and phase transitions in two-dimensional systems. *Journal of Physics C: Solid State Physics*, 6(7):1181–1203, apr 1973.

[3] Siamak Dadras, Alexander Gresch, Caspar Groiseau, Sandro Wimberger, and Gil S. Summy. Quantum walk in momentum space with a bose-einstein condensate. *Phys. Rev. Lett.*, 121:070402, Aug 2018.

[4] Siamak Dadras, Alexander Gresch, Caspar Groiseau, Sandro Wimberger, and Gil S Summy. Experimental realization of a momentum-space quantum walk. *Physical Review A*, 99(4):043617, 2019.

[5] Longwen Zhou and Jiangbin Gong. Floquet topological phases in a spin-1/2 double kicked rotor. *Phys. Rev. A*, 97:063603, Jun 2018.

[6] Caspar Groiseau, Alexander Wagner, Gil S. Summy, and Sandro Wimberger. Impact of lattice vibrations on the dynamics of a spinor atom-optics kicked rotor. *Condensed Matter*, 4(1), 2019.

[7] Philipp M Preiss, Ruichao Ma, M Eric Tai, Alexander Lukin, Matthew Rispoli, Philip Zupancic, Yoav Lahini, Rajibul Islam, and Markus Greiner. Strongly correlated quantum walks in optical lattices. *Science*, 347(6227):1229–1233, 2015.

[8] Wolfgang Dür, Robert Raussendorf, Viv M Kendon, and H-J Briegel. Quantum walks in optical lattices. *Physical Review A*, 66(5):052319, 2002.

[9] Kai Eckert, J Mompart, Gerhard Birkl, and Maciej Lewenstein. One-and two-dimensional quantum walks in arrays of optical traps. *Physical Review A*, 72(1):012327, 2005.

[10] Andreas Steffen, Andrea Alberti, Wolfgang Alt, Noomen Belmechri, Sebastian Hild, Michał Karski, Artur Widera, and Dieter Meschede. Digital atom interferometer with single particle control on a discretized space-time geometry. *Proceedings of the National Academy of Sciences*, 109(25):9770–9774, 2012.

[11] Thorsten Groh, Stefan Brakhane, Wolfgang Alt, Dieter Meschede, Janos K Asbóth, and Andrea Alberti. Robustness of topologically protected edge states in quantum walk experiments with neutral atoms. *Physical Review A*, 94(1):013620, 2016.

[12] Michal Karski, Leonid Förster, Jai-Min Choi, Andreas Steffen, Wolfgang Alt, Dieter Meschede, and Artur Widera. Quantum walk in position space with single optically trapped atoms. *Science*, 325(5937):174–177, 2009.

[13] CM Chandrashekar. Implementing the one-dimensional quantum (hadamard) walk using a bose-einstein condensate. *Physical Review A*, 74(3):032307, 2006.

[14] Ben C Travaglione and Gerald J Milburn. Implementing the quantum random walk. *Physical Review A*, 65(3):032310, 2002.

[15] F Zähringer, G Kirchmair, R Gerritsma, E Solano, R Blatt, and CF Roos. Realization of a quantum walk with one and two trapped ions. *Physical review letters*, 104(10):100503, 2010.

[16] Hector Schmitz, Robert Matjeschk, Ch Schneider, Jan Glueckert, Martin Enderlein, Thomas Huber, and Tobias Schaetz. Quantum walk of a trapped ion in phase space. *Physical Review Letters*, 103(9):090504, 2009.

[17] David J Wineland, C Monroe, Wayne M Itano, Dietrich Leibfried, Brian E King, and Dawn M Meekhof. Experimental issues in coherent quantum-state manipulation of trapped atomic ions. *Journal of Research of the National Institute of Standards and Technology*, 103(3):259, 1998.

[18] Hagai B Perets, Yoav Lahini, Francesca Pozzi, Marc Sorel, Roberto Morandotti, and Yaron Silberberg. Realization of quantum walks with negligible decoherence in waveguide lattices. *Physical Review Letters*, 100(17):170506, 2008.

[19] Alberto Peruzzo, Mirko Lobino, Jonathan CF Matthews, Nobuyuki Matsuda, Alberto Politi, Konstantinos Poulios, Xiao-Qi Zhou, Yoav Lahini, Nur Ismail, Kerstin Wörhoff, et al. Quantum walks of correlated photons. *Science*, 329(5998):1500–1503, 2010.

[20] Filippo Cardano, Alessio D'Errico, Alexandre Dauphin, Maria Maffei, Bruno Piccirillo, Corrado de Lisio, Giulio De Filippis, Vittorio Cataudella, Enrico Santamato, Lorenzo Marrucci, et al. Detection of zak phases and topological invariants in a chiral quantum walk of twisted photons. *Nature Communications*, 8:15516, 2017.

[21] Chao Chen, Xing Ding, Jian Qin, Yu He, Yi-Han Luo, Ming-Cheng Chen, Chang Liu, Xi-Lin Wang, Wei-Jun Zhang, Hao Li, et al. Observation of topologically protected edge states in a photonic two-dimensional quantum walk. *Physical review letters*, 121(10):100502, 2018.

[22] Hao Tang, Xiao-Feng Lin, Zhen Feng, Jing-Yuan Chen, Jun Gao, Ke Sun, Chao-Yue Wang, Peng-Cheng Lai, Xiao-Yun Xu, Yao Wang, et al. Experimental two-dimensional quantum walk on a photonic chip. *Science advances*, 4(5):eaat3174, 2018.

[23] Konstantinos Poulios, Robert Keil, Daniel Fry, Jasmin DA Meinecke, Jonathan CF Matthews, Alberto Politi, Mirko Lobino, Markus Gräfe, Matthias Heinrich, Stefan Nolte, et al. Quantum walks of correlated photon pairs in two-dimensional waveguide arrays. *Physical Review Letters*, 112(14):143604, 2014.

[24] Andreas Schreiber, Katiuscia N Cassemiro, Václav Potoček, Aurél Gábris, Peter J Mosley, Erika Andersson, Igor Jex, and Ch Silberhorn. Photons walking the line: a quantum walk with adjustable coin operations. *Physical review letters*, 104(5):050502, 2010.

[25] Vivien M Kendon. A random walk approach to quantum algorithms. *Philosophical Transactions of the Royal Society A: Mathematical, Physical and Engineering Sciences*, 364(1849):3407–3422, Oct 2006.

[26] Adrian Ortega, Thomas Gorin, and Craig S. Hamilton. Quantum transport in a combined kicked rotor and quantum walk system. *Physics Letters A*, 395:127224, 2021.

[27] Marcel Weiß, Caspar Groiseau, W. K. Lam, Raffaella Burioni, Alessandro Vezzani, Gil S. Summy, and Sandro Wimberger. Steering random walks with kicked ultracold atoms. *Physical Review A*, 92(3), Sep 2015.

[28] Alexander Lukas Wagner. Topology in 1d quantum walks, Bachelor thesis 2018. [`https://www.thphys.uni-heidelberg.de/~wimberger/theses.html`].

[29] C Groiseau, A Gresch, and S Wimberger. Quantum walks of kicked bose–einstein condensates. *Journal of Physics A: Mathematical and Theoretical*, 51(27):275301, jun 2018.

[30] C Groiseau. Discrete-time quantum walks in momentum space. Master's thesis, 2017.

[31] Jiating Ni, Wa Kun Lam, Siamak Dadras, Mario F Borunda, Sandro Wimberger, and Gil S Summy. Initial-state dependence of a quantum resonance ratchet. *Physical Review A*, 94(4):043620, 2016.

[32] Jiating Ni, Siamak Dadras, Wa Lam, Rabi Shrestha, Mark Sadgrove, Sandro Wimberger, and Gil Summy. Hamiltonian ratchets with ultra-cold atoms. *Annalen der Physik*, 529:1600335, 07 2017.

[33] Kai Bongs and Klaus Sengstock. Physics with coherent matter waves. *Reports on Progress in Physics*, 67, 03 2004.

[34] Takuya Kitagawa. Topological phenomena in quantum walks; elementary introduction to the physics of topological phases, 2011.

[35] This information stems from a discussion with Yingmei Liu and Jerry Clark, representing the experimental team at Oklahoma university working on potentially measuring the topological phase transitions.

[36] Milton Abramowitz and Irene A Stegun. *Handbook of mathematical functions with formulas, graphs, and mathematical tables*, volume 55. US Government printing office, 1964.

Erklärung

Hiermit versichere ich, dass ich diese Arbeit selbstständig verfasst habe. Neben den angegebenen Quellen und Hilfsmitteln habe ich keine weiteren verwendet.

Heidelberg, den 25 Februar, 2022